Extrusion tectonism of Indochina reassessed: constraints from ^{40}Ar/^{39}Ar geochronology from the Day Nui Con Voi metamorphic massif, Vietnam

Thi-Hue Dinh[1], Meng-Wan Yeh[2]*, Tung-Yi Lee[2], Michael J. Kunk[3], Robert P. Wintsch[4] and Ryan McAleer[3]

[1]Department of Earth Sciences, National Central University, Taoyuan City, Taiwan, [2]Department of Earth Sciences, National Taiwan Normal University, Taipei City, Taiwan, [3]U.S. Geological Survey, Florence Bascom Geoscience Center, Reston, VA, United States, [4]Department of Earth and Environmental Sciences, Wesleyan University, Middletown, CT, United States

The extrusion tectonic model for the southeastern margin of the Himalayan orogeny links the crustal shear activity along the Red River Shear Zone (RRSZ) to the opening of the South China Sea (SCS). The Day Nui Con Voi (DNCV) metamorphic massif in northern Vietnam strikes NW-SE, is bounded by the RRSZ to the south and continues along the strike where it meets the SCS. The DNCV is thus a critical area to document thermotectonic history in order to advance our understanding of the tectonic evolution of Indochina extrusion and its relationship to the opening of the SCS. Our new ^{40}Ar/^{39}Ar data combined with microstructural and petrological analyses constrained the timing of the left-lateral shearing of the RRSZ and revealed the thermal evolution of the DNCV metamorphic massif. Three ductile deformation events were observed. D_1 formed NNW-SSE striking upright folds under granulite to upper amphibolite facies conditions. D_2 was a horizontal to sub-horizontal folding event that occurred at amphibolite facies conditions. D_3 was a doming event that formed NW-SE striking up-right folds bounded by left-lateral shearing mylonite belts along the two limbs. The S/C fabrics were defined by muscovite fish, quartz + albite + K-feldspar aggregates, and muscovite folia. The D_3 doming event exhumed the DNCV metamorphic massif from amphibolite facies conditions to the lower greenschist facies conditions. The ^{40}Ar/^{39}Ar ages obtained from amphibole (~26 Ma), phlogopite (~25 Ma), muscovites (~24-23 Ma), biotite (~25-23 Ma), and K-feldspars (~25-22 Ma) from different structural domains of the DNCV metamorphic massif indicated a rapid exhumation ~26−22 Ma. We interpreted this as the time period for the D_3 event, with the onset of left-lateral shearing occurring around 24 Ma based on ages obtained from syn-kinematic muscovites. This age was much younger than the initiation of sea-floor spreading of the SCS (since 32 Ma) but coincided with the age for the ridge jump event in the SCS. Based on these new data, we proposed that extrusion tectonism cannot be the cause for the initial opening of the SCS. Rather, the extrusion of the Indochina block was temporally correlative with the southward ridge jump event of the already opened SCS.

1 Introduction

The potential oil and gas reserves in the South China Sea (SCS) have attracted much research into the formation and evolution of the SCS over the past few decades (e.g., Dung et al., 2012; Hall, 2002; Sun, 2016; Tapponnier et al., 1982; tapponnier et al., 1986; Taylor and Hayes, 1980; Mai et al., 2018; Ye et al., 2018). To explain how the SCS was formed, many tectonic models have been proposed, such as the back-arc extension model (e.g., Karig, 1971; Avraham and Uyeda, 1983; Mai et al., 2018), the indentation-extrusion model (e.g., Tapponnier et al., 1982; tapponnier et al., 1986), and the subduction of the proto-SCS model (e.g., Hall, 1997; Hall, 2009; Longley, 1997; Morley, 2002). Among them, the indentation-extrusion model has received the most attention. In this model, the southeastward extrusion of the Indochina block accommodated by left-lateral movement along the RRSZ was considered the cause for the opening of the SCS (Figure 1A) (Tapponnier et al., 1982; tapponnier et al., 1986). The key supporting evidence to the indentation-extrusion model is the contemporaneity between the left-lateral movement along the RRSZ (ca. 35 to 17 Ma, Leloup and Kienast, 1993; Zhang and Schärer, 1999) and the sea-floor spreading in the SCS (ca. 32 to 15.5 Ma, Briais et al., 1993; Lee and Lawver, 1995). Various methods were applied to constrain the timing of the left-lateral movement in the RRSZ. Absent in this model, however,

is a significant consideration of driving forces for plate movements. Based on Wilson cycle, a continental crust must first be thinned for rifting to take place. Strike-slip motion on steeply dipping and relatively narrow fault zones does not provide enough structural softening to significantly lower the strength of the continental crust outside of the shear belt, and so will not, by itself, initiate regional crustal thinning. Furthermore, the density of the continental crust is approximately 2.7 g/cm^3, much less dense than the oceanic crust, which is approximately 3.0 g/cm^3 (e.g., Christopherson et al., 2009). Because of its relatively lower density, the light and buoyant continental crust is unlikely to be the causal mechanism to push and open a new oceanic crust (Girdler, 1965). Additionally, Mai et al. (2018) conducted a temporal and geographical reconstruction of Cretaceous and Cenozoic magmatism within the SE margin of Eurasia with the isochrones of major basins within the SCS, and concluded: 1) the rollback of the paleo-pacific sea plate is the main crustal thinning mechanism along the southeastern boundary of Eurasia, and 2) the 3,000 km long north dipping subduction belt of Neo-Tethys stretching from Burma–Andaman block to Sumatra should be a more plausible candidate for the opening of the SCS.

Initial geochronologic research suggested left-lateral activity on the RRSZ from ~35–17 Ma; almost exactly coincident with sea-floor spreading in the SCS. In brief, U-Pb and ^{40}Ar/^{39}Ar ages between 35 and 17 Ma were obtained for zircon, monazite,
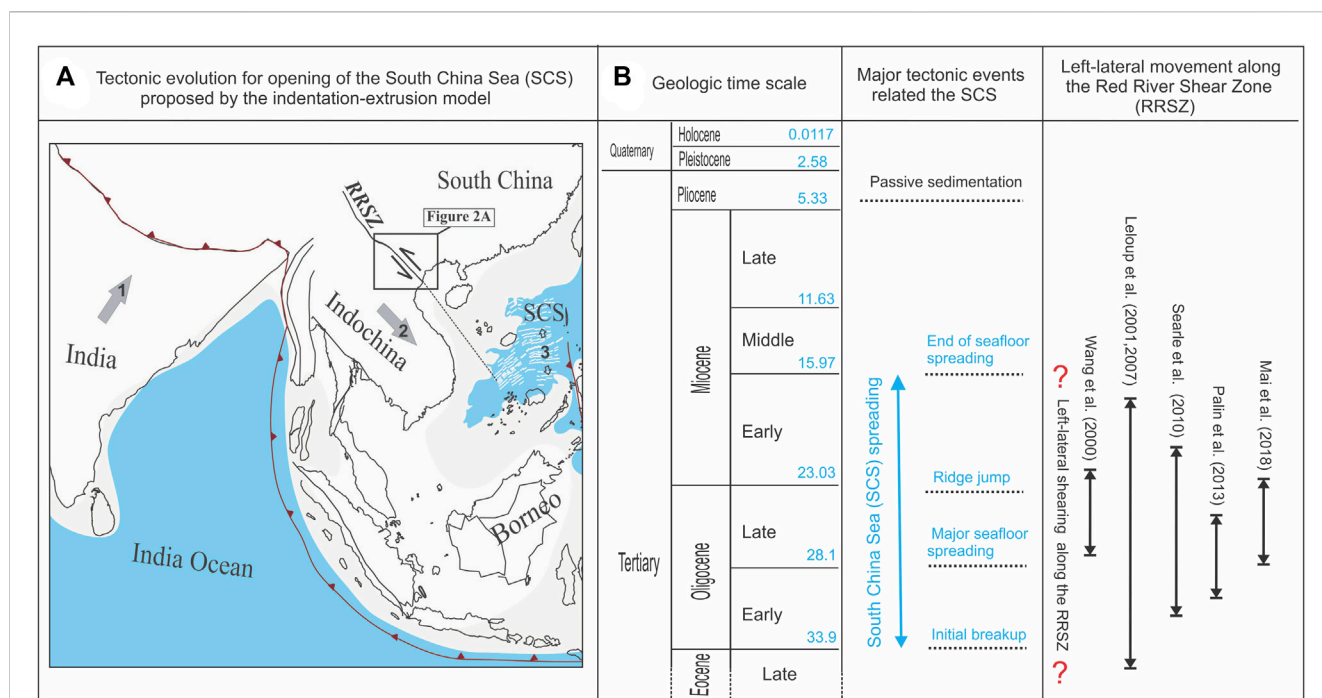
FIGURE 1
(A) Stretch map shows the time sequence following the indentation-extrusion model (Tapponnier et al., 1982; 1986), indicated by the India-Eurasia collision first, then by the southeastward extrusion of the Indochina block along the RRSZ, and finally by the opening of the SCS. The numbers represent the order of tectonic events. Black rectangles indicate the location of northern Vietnam (Figure 2A). **(B)** Schematic diagram showing major tectonic events related to the opening of the South China Sea (SCS) and the proposed timing of left-lateral movement along the Red River Shear Zone (RRSZ) from a previous study. The shearing was constrained from ca. 27–22 Ma (^{40}Ar-^{39}Ar data; Wang et al., 2000); 35–17 Ma (U-Pb and ^{40}Ar-^{39}Ar data; Leloup et al., 2001; 2007); 32–22 Ma (structural and geochronological data; Searle et al., 2010); 31–25 Ma (geochronological and petrological data; Palin et al., 2013); 28–23 Ma (tectonic reconstructions; Mai et al., 2018).

FIGURE 2
(A) Tectonic sketch showing the location of major strike-slip faults (red lines) in northwestern Vietnam and the location of the study area (black rectangle). **(B)** Geological map (Modified from 1:1,500,000 geological map, General Geological Department of Vietnam, 1983) with previously reported ^{40}Ar/^{39}Ar ages and U-Pb zircon ages within Day Nui Con Voi massif and surrounding areas. **(C)** Two cross-sections of the Bao Yen- Bao Ha and Mau A transects across the Day Nui Con Voi massif show different deformation events. S_1 is the fold axial plane of the oldest deformation event (D_1). The second deformation event (D_2) folded the S_1 axial plane, forming the S_2 fold axial plane. This plane was folded and deformed by a later deformation event (D_3), represented by the S_3 fold axial plane.

hornblende, biotite, and titanite from granitic rocks near the shear zone (Leloup and Kienast, 1993; Zhang and Schärer, 1999; Leloup et al., 2001; Leloup et al., 2007). However, later studies by Wang et al. (2000), Searle (2006), and Searle et al. (2010) pointed out that most of the granitic rocks are pre-kinematics and so U/Pb zircon ages provide only a maximum age for the initiation of left-lateral motion on the RRSZ. Additionally, recent studies (Junlai et al., 2020; Gou et al., 2021; Li et al., 2021) concluded that these granitic melts were formed as a product of the crustal collapse of the thickened crustal lithosphere and that this

magmatism may have helped to weaken the lithosphere, facilitating the initiation of movement along the RRSZ. In other words, these dated granitic rocks were emplaced prior to the tectonic extrusion of the Indochina block. The crystallization age of those magmas should not be conflated with the timing of left-lateral movement along the RRSZ.

Different time ranges for motion on the RRSZ have been proposed by different authors, such as ca. 32–22 Ma by Searle et al. (2010), ca. 31–25 Ma by Palin et al. (2013), ca. 27–22 Ma by Wang et al. (2000), and ca. 28–23 Ma by Mai et al. (2018), as

presented in Figure 1B. Clearly, debates remain over the actual timing of the left-lateral movement along the RRSZ, and the mechanism for extrusion of the Indochina block and its linkage to the opening of the SCS need further examination. This study re-examines the timing of left-lateral movement along the RRSZ by sampling across the DNCV metamorphic massif, which is critical for assessing the true temporal and kinematic relationship of extrusion of the Indochina block and tectonic evolution of the SCS.

2 Geological background

The RRSZ is one of the largest strike-slip shear zones in SE Asia, stretching from the southeastern corner of the Tibetan plateau to the SCS (Figure 1). There is a sequence of granitic rocks and four metamorphic massifs distributed along and near the RRSZ. Zircon U-Pb dating studies indicated at least three generations for granitic rocks within and surrounding the shear zone (Figure 2). The first generation occurred at ca. 760-730 Ma (Duong et al., 2021) and produced partial melting of surrounding rocks during the Neoproterozoic Jinning orogeny. The second generation of granitic rocks crystallized at ca. 261–245 Ma (Carter et al., 2001; Usuki et al., 2015; Shellnutt et al., 2020) and may relate to magmatism during the Permian-Triassic Indosinian orogeny. The third generation is represented by granitic rocks with zircon U-Pb ages of ca. 35 Ma (Zhang and Schärer, 1999). This Late Eocene magmatism is related to the India-Eurasia collision event. The four metamorphic massifs distributed along the RRSZ are the Xuelong Shan, Diancang Shan, the Ailao Shan massifs in China, and the DNCV in Vietnam. The metamorphic massifs display gneiss dome-like structures, with medium to high-grade gneiss and amphibolite within their cores bounded by low-grade schist and mylonite belts along both limbs (Yeh et al., 2008; 2014; Wu et al., 2017; Liu et al., 2020).

The DNCV metamorphic massif is in the southeastern most segment of the RRSZ and strikes in an NW-SE direction. It is approximately 30 km wide and more than 250 km long, extending from Lao Cai to Viet Tri city, in northern Vietnam. At its northern extent (near Lao Cai city), the DNCV metamorphic massif is a gneiss dome structure and nearly connects to the Ailao Shan metamorphic massif (Figure 2). The southern portion is covered by Neogene-Quaternary sediments in the south near the city of Viet Tri. The DNCV metamorphic massif is bounded by two steep normal faults of the Red River Fault along the SW limb and the Chay River Fault along the NE limb (Leloup et al., 1995) (Figure 2). The DNCV metamorphic massif is composed mainly of amphibolite, mylonite, garnet-biotite-sillimanite gneiss, garnet-biotite gneiss, two mica-garnet schists with garnet, and small lenses of marble. Petrological and geothermal-barometric studies indicated that two main periods of metamorphism and deformation occurred in the DNCV metamorphic massif (Nam et al., 1998; Yeh et al., 2008). The first period relates to the peak metamorphism, and reached upper amphibolite facies condition with calculated temperature and pressure ranges of 650–830°C and 5–9 kbar, respectively (Nam et al., 1998; Gilley et al., 2003; Anczkiewicz et al., 2007; Khoi et al., 2016). The second period of metamorphism and deformation occurred in greenschist facies with a peak temperature of ~480°C and <3 kbar

(Nam et al., 1998) as a result of retrograde processes. The high-grade metamorphism was initially considered to be synchronous with left-lateral shearing along the RRSZ resulting from shear heating (Leloup et al., 2007). Yeh et al. (2008) deciphered three deformation events accompanied by regional metamorphism under the mid-crustal level since the Triassic Indosinian orogeny. However, other than the establishment of these deformation events are pre-left lateral shearing (Yeh et al., 2008; Yeh et al., 2014; Searle et al., 2010). The actual timing of these upright folding (D_1), recumbent folding (D_2), and gneiss doming (D_3) events is uncertain. Existing and new geochronologic and thermochronologic data need to be interpreted within the context of this newly deciphered structural and metamorphic evolution.

3 Materials and methods

Microstructural and petrological analyses were carried out from the oriented thin sections by using optical and cathodoluminescence (CL) petrography at the Department of Earth Sciences, National Taiwan Normal University. Electron microscopy was carried out by using a Camera SX-50 electron microprobe to determine characteristic mineral assemblages and microstructural evidence for the sequence of deformation events. CL images were taken using a Leica DM LP petrographic microscope equipped with CITL CCL8200mk3 CL stage under an acceleration potential of 12 kV, a beam current of 700 A, and an exposure time of 30 s. Based on cross-cutting relationships observed from the field and the oriented thin sections, different deformation events occurring in the study area were distinguished and a relative structural history was reconstructed. Within the context of this detailed microstructural and petrological analysis, $^{40}Ar/^{39}Ar$ dating of different minerals was also carried out. Thirteen samples of mineral separates from different lithologies, including biotite gneiss, amphibolite, schist, and mylonite (Table 1), were analyzed using the $^{40}Ar/^{39}Ar$ furnace step-heating method on either a VG MM 1200b or MAP 216 mass spectrometer at the U.S. Geological Survey argon dating laboratory, Reston, Virginia, following procedures stated in Haugerud and Kunk (1988) and Kunk et al. (2005). The samples were crushed and ground in the jaw crusher and disk mill, respectively. The minerals of interest were then concentrated to an optical purity of >99% via standard magnetic and density separation techniques. Aliquots of the separates were packaged in high-purity copper and then irradiated in the TRIGA reactor (GSTR) at the U.S. Geological Survey, Denver, Colorado for 20 MWh along with Fish Canyon Tuff sanidine (28.201 ± 0.046 Ma; Kuiper et al., 2008) as the monitor mineral, or for 40 MWh (1 of 14 samples) along with MMHB hornblende (527 Ma; Schmitz, 2012). Following irradiation, the mineral packets were incrementally heated in a low-blank furnace for 10–15 min per heating step, with schedules varying between 10 and 16 steps.

Data reduction was accomplished using an updated version of Ar-Ar* (Haugerud and Kunk, 1988) or MassSpec (Deino, 2014), the decay constants of Min et al. (2000), and atmospheric argon isotopic abundances of Lee et al. (2006). A plateau age was calculated here when three or more contiguous steps agreed at 2σ and

TABLE 1 Sample list and age summaries obtained from mineral separates of different samples with lithology and location information (** indicates does not meet all criteria for age plateau. Criteria not meet are in italics.).

| Sample no. | Lithology | Location | | Dated minerals | LabID | Min age (Ma) | Max age (Ma) | Plat age (Ma) | 2 sigma | ^{39}Ar % | Steps | MSWD | Integ age (Ma) | Isoch age (Ma) | Prefe-rred Age (Ma) | Instrument |
		Lon (E)	Lat (N)													
K10-11-07A	Amphibolite			Biotite	73KD57	24.7	26.4	24.9**	0.2	94.8	10	3.5	24.9	Na	24.7	VG1200
K10-11-07A1	Leucogranitic dyke			Biotite	28KD59	23.3	26.6	25.0	0.4	99.9	10	0.99	26.4	24.9	25.0	MAP216
				K-Feldspar	107KD57	23.0	27.2	Na					26.2	Na	23.0	VG1200
K10-11-07A2	Biotite +Garnet Augen Gneiss	104.911°	21.797°	K-Feldspar	30KD57	22.7	27.6	24.6	0.2	61.2	3	1.5	25.0	23.3	24.6	MAP216
K10-11-07A3	Phlogopite bearing Marble			Phlogopite	46KD57	24.7	26.2	25.0	0.2	99.8	17	1.3	25.3	25.0	25.0	MAP216
K10-11-07C	K-feldspar vein			Muscovite	92KD57	23.88	24.87	24.3	0.2	100	18	1.0	24.4	24.3	24.3	MAP216
		104.360°	22.180°	K-feldspar	97KD57	21.5	25.8	Na					24.6	Na	21.45	VG1200
K10-11-07C1	Phyllite			Muscovite	44KD57	22.6	37.2	24.5	0.2	82.3	9	1.6	24.1	24.3	24.5	MAP216
K10-11-07D	Muscovite bearing Mylonite	104.359°	22.180°	K-feldspar	28KD57	22.3	39.2	Na					31.6	Na	23.0	MAP216
K10-11-08A	Amphibolite	104.367°	22.181°	Amphibole	126KD57	26.5	27.8	26.6	0.1	56.9	2		27.3	Na	26.5	VG1200
K10-11-08B	Muscovite bearing Pegmatitic vein			Muscovite	100KD57	22.9	25.3	23.3	0.2	73.1	7	2.31	23.5	23.1	23.3	MAP216
		104.394°	22.196°	K-feldspar	104KD57	23.7	38.9	Na					29.6	Na	23.7	MAP216
K10-11-08B1B	Garnet+sillimanite+biotite Mylonite			Biotite	88KD57	22.8	35.8	Na					25.4	Na	22.8	MAP216
K10-11-08E	Muscovite bearing Mylonite	104.585°	22.174°	Muscovite	102KD57	22.4	24.8	23.5	0.3	99.9	16	0.9	23.4	23.3	23.5	MAP216
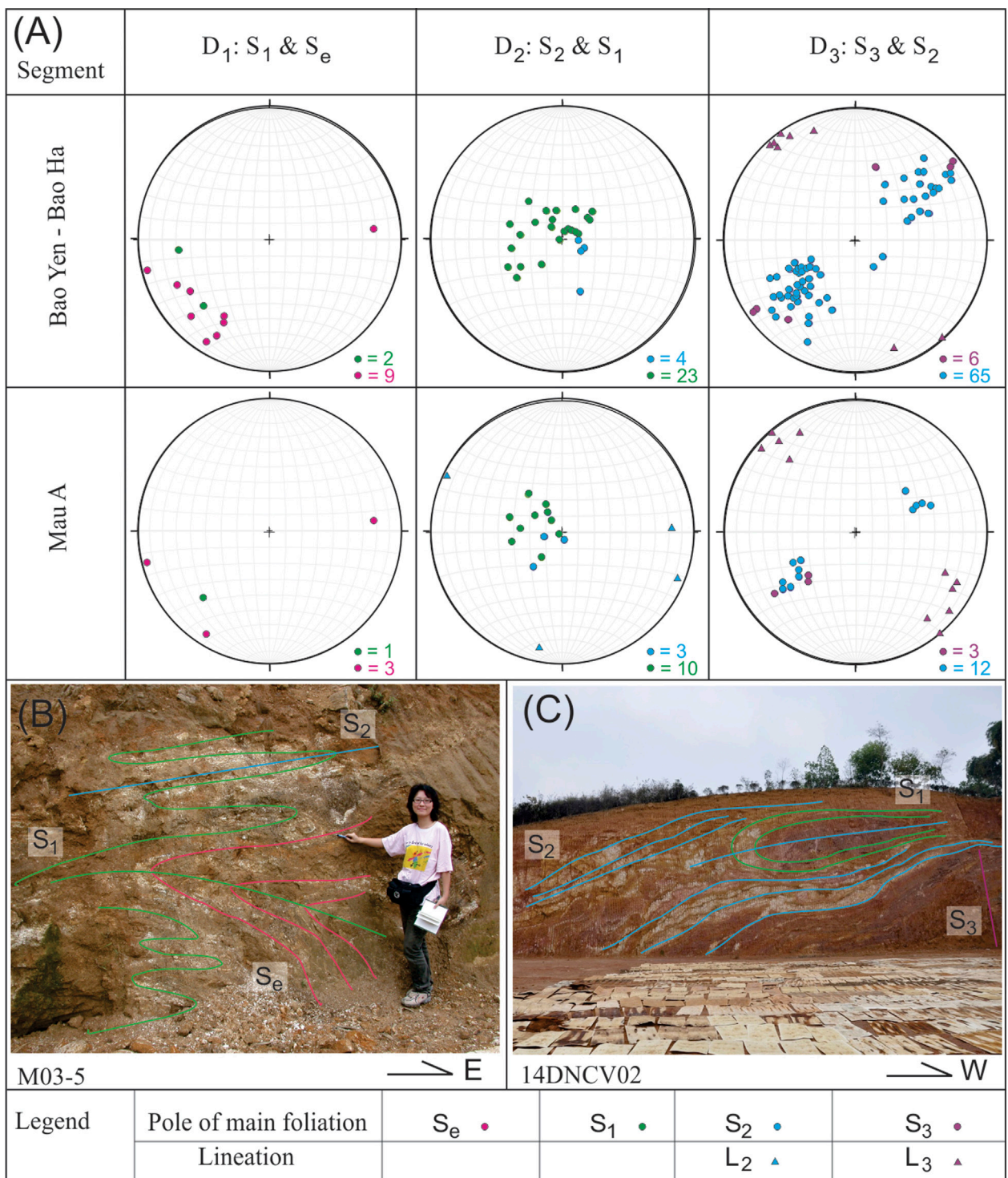
FIGURE 3
(A) Equal area stereographic projections (S hemisphere) of poles to S_e, S_1, S_2, S_3 foliation planes and lineation corresponding to different deformation events D_1, D_2, D_3 from the Bao Yen-Bao Ha and Mau A transects and field photos showing relationship of different deformations in the outcrops M03-5 **(B)** and 14DNCV02 **(C)**.

included >60% of the ^{39}Ar. In several instances, age spectra were "flat" but did not meet the above statistical criteria. In these cases, a preferred weighted average age was used and the relevant statistics are reported in Table 1. Production rates for reactor-induced

interfering isotopes were those listed by Cassel et al. (2009). Errors in preferred ages included analytical errors in analysis, decay factor uncertainties, measured atmospheric or calculated initial ^{40}Ar/^{36}Ar ratios, the irradiation parameter J, the
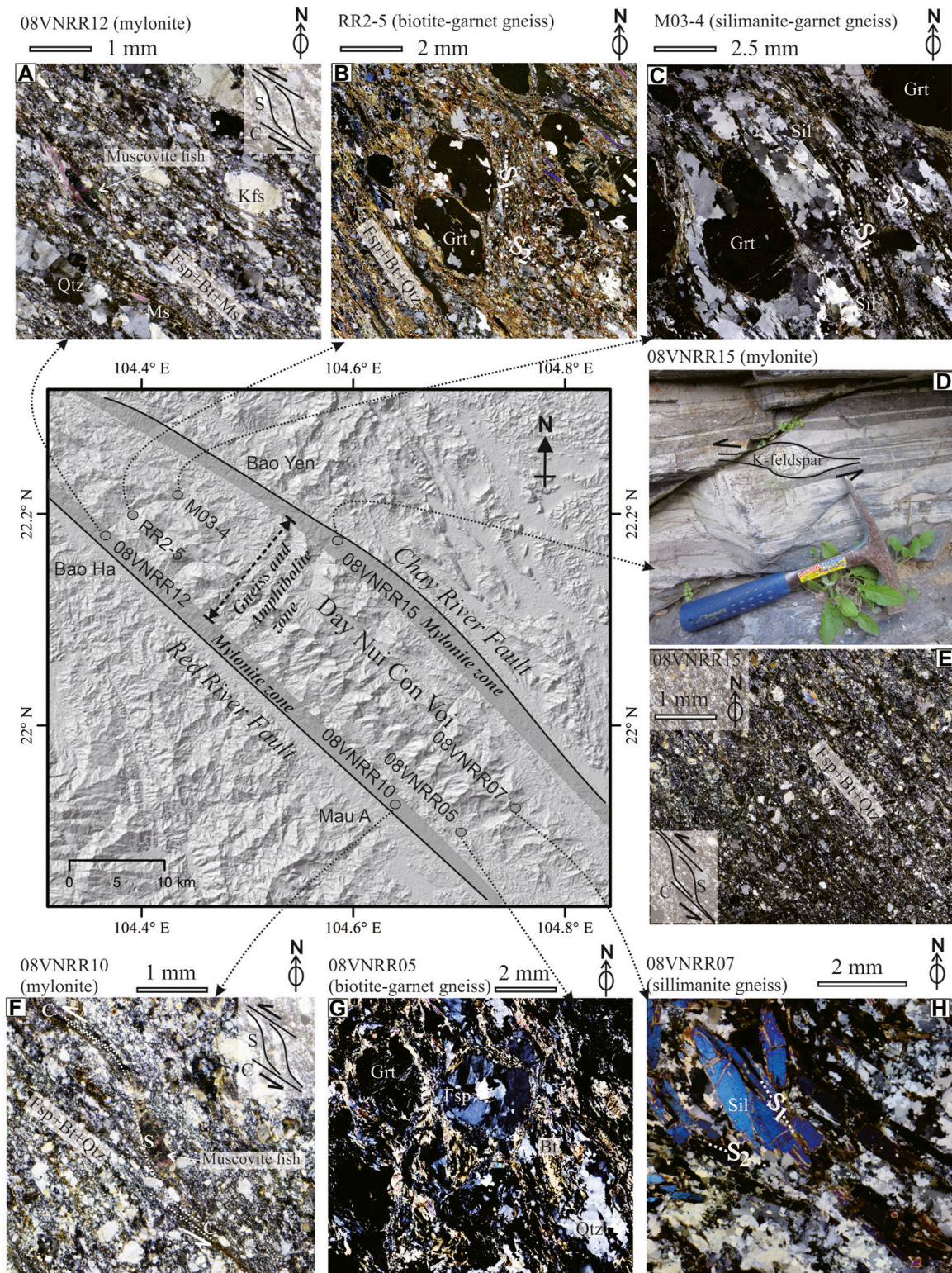
FIGURE 4
Shaded relief map showing dome-like structure with boundary mylonitic zones and sample location for petrological analysis. Representative field photographs and related microphotographs illustrate different metamorphic conditions presented by different rock types changing from the core to the rims of the Day Nui Con Voi metamorphic massif. The dominant rocks in the core of the massif are gneiss with foliation defined by the orientation of quartz ribbon, feldspar, mica folia, and sillimanite (RR2-5, M03-4, 08VNRR05, 08VNRR07) **(B, C, G, H)**. Garnet porphyroblasts are wrapped and truncated by all matrix foliation **(B, C, G)**. The dominant rock type is mylonite and phyllite for both limbs of the massif **(A, D, E, F)**. As represented in samples 08VNRR10, 08VNRR12, 08VNRR15 showing fine-sized grains of quartz, feldspar, and muscovite defining S/C fabrics. Mineral abbreviations: Bt- biotite; Fsp- feldspar; Kfs- K-feldspar; Grt- garnet; Ms- muscovite; Qtz- quartz; Sil- sillimanite.

production ratios of the various reactors that induced argon-producing reactions, and the uncertainty in the age of the monitor mineral. Additional data reduction parameters as well as complete isotopic data can be found in the Supplementary Tables and in the work by Dinh et al. (2023).

General guidelines for $^{40}Ar/^{39}Ar$ age data reporting that were described by Schaen et al. (2020) were followed. A relatively high diffusion rate through multi-domains is a common feature for argon systems at the middle and lower crust level. That makes the determination of closure temperatures of obtained $^{40}Ar/^{39}Ar$ ages a challenging issue for minerals that went through stable or slowly cooled thermal conditions such as in the case of plutonic or metamorphic rocks. By assuming the cooling pattern was linear and monotonic, we estimated the bulk closure temperatures using Eq. 1 (Dodson, 1973; Schaen et al., 2020).

$$T_c = \frac{E}{Rln\left(AD_oRT_c/a^2E\left(dT/dt\right)\right)} \quad (1)$$

Where E is the activation energy, R is the gas constant, and A is a numeral constant that depends on the model geometry that represents the best diffusion of ^{40}Ar within the mineral. Values of 55, 27, or 8.7 for diffusion from a sphere, cylinder, or plane sheet can be assigned respectively. D_0 is a pre-exponential constant in the Arrhenius equation, a is the diffusion size, and dT/dt is the assumed cooling rate. As Lovera et al. (1991) pointed out, a smaller diffusion size (a) than grain size should be utilized if subgrains are observed. Therefore, we utilized an assumed diffusion domain size (a) of 100 μm, and a rapid cooling rate from 50°C/Ma to 100°C/Ma to gain the maximum and minimum bulk cooling temperature ranges.

4 Results and interpretations

4.1 Reconstructed structural and petrological evolution of the DNCV metamorphic massif

In order to determine the structural and metamorphic history of the DNCV metamorphic massif, two mapping transects across the width of the DNCV metamorphic massif were made. These transects are here termed the Bao Ha - Bao Yen transect and the Mau A transect (Figures 2, 3). Each transect records the same general structural history, and so observations from both transects were included when discussing the composite history of the DNCV metamorphic massif. The core region of the DNCV metamorphic massif mainly consists of garnet + biotite + sillimanite gneiss with interlayered amphibolite. The foliations are horizontal to sub-horizontal and recumbent folds are common. Petrographically, the foliations are well-defined by the aligned sillimanite, biotite, and quartz ribbons (Figures 4B, C, G, H). The matrix foliation becomes steeper toward the margins of the DNCV metamorphic massif resulting in a dome-like structure. The two limbs of the massif are characterized by mylonite zones that range from 10 to 200 m in width. Both margins display well-defined S/C fabrics that are typically defined by muscovite fish with a left-lateral sense of shear, and biotite folia and quartz and feldspar aggregates (Figures

4A, D, E, F). Three ductile deformation events were reconstructed through our field and microstructural analyses and are discussed in more detail below.

4.1.1 D_1 deformation event

The oldest deformation event, D_1, formed centimeter to meter scale NNW-SSE striking upright folds that folded the pre-existing metamorphic layering (S_e). These F_1 folds have a sub-vertical to steep NE dipping axial plane (S_1). The hinges of the centimeter to meter scale upright F_1 folds that were truncated by sub-horizontal foliation (S_2) were observed in a few outcrops. Almost all of them were refolded and deformed by later deformations (e.g., Figure 3B). The reported orientation of S_1 was based on the rare examples where F_1 folds appeared largely unaffected by later deformation events. In thin sections, the S_1 foliation was defined by the alignment of sillimanite and biotite within the cleavage domain, and quartz and feldspar aggregates defined the microlithon domain for gneiss samples (Figures 4B, C, G, 5C). Garnet porphyroblasts were observed within the microlithon domain and were wrapped and/or truncated by all matrix foliations, suggesting garnet growth occurred pre-to syn-D_1 (Figures 5A, C). The mineral assemblage of quartz, K-feldspar, biotite, garnet, and sillimanite was commonly referred to as a granulite facies assemblage (Froese, 1973). Myrmekite was also commonly observed. In the CL image (Figure 5B), K-feldspar appears dark blue against pale green myrmekite growth, which is parallel to S_1 foliation (Figures 5A, B). The development of pre-to post-plagioclase myrmekite suggests that the D_1 deformation event occurred at a high temperature of more than 550°C (e.g., Wirth and Voll, 1987; Cesare et al., 2002). The mineral assemblage of sillimanite, biotite, quartz, and feldspars along with the pre-to syn-D_1 growth of garnet suggests that the following reaction likely occurred:

Garnet + K-feldspar +Liquid → Biotite + Sillimanite + quartz (Froese, 1973).

This further constrained the temperature of the D_1 deformation event from granulite facies to upper amphibolite facies (800°C–650°C).

4.1.2 D_2 deformation event

The D_2 deformation event was associated with sub-horizontal to inclined folds that were centimeters to a few meters in scale and had a horizontal axial plane (S_2, Figures 3B, C). The poles of folded S_1 foliations and S_2 fold axial planes are marked by green and blue circles, respectively, as shown in Figure 3A. The blue triangles mark the mineral stretching lineation, show a general ESE-WNW trend, and plunge shallowly (<10°) to the ESE and WNW. Microstructural and petrological analyses indicated that the S_2 foliation was well-defined by sillimanite and biotite folia, quartz, and feldspar (Figures 5A, C, D, 6A). Quartz commonly forms ribbons and finer grains with irregular grain boundaries and undulose extinction (Figures 5A, C, 6A). Euhedral sillimanite and subhedral biotite were in textural equilibrium and had long axes parallel to the S_2 foliation (Figure 5D). Muscovite, which is only present in pegmatites, is was texturally late, and appeared to replace K-feldspar. These observations indicated muscovite was absent in the D_2 assemblage (e.g., Figure 5A). Mineral assemblages of sillimanite + biotite + high deformed quartz and feldspar suggested that the D_2
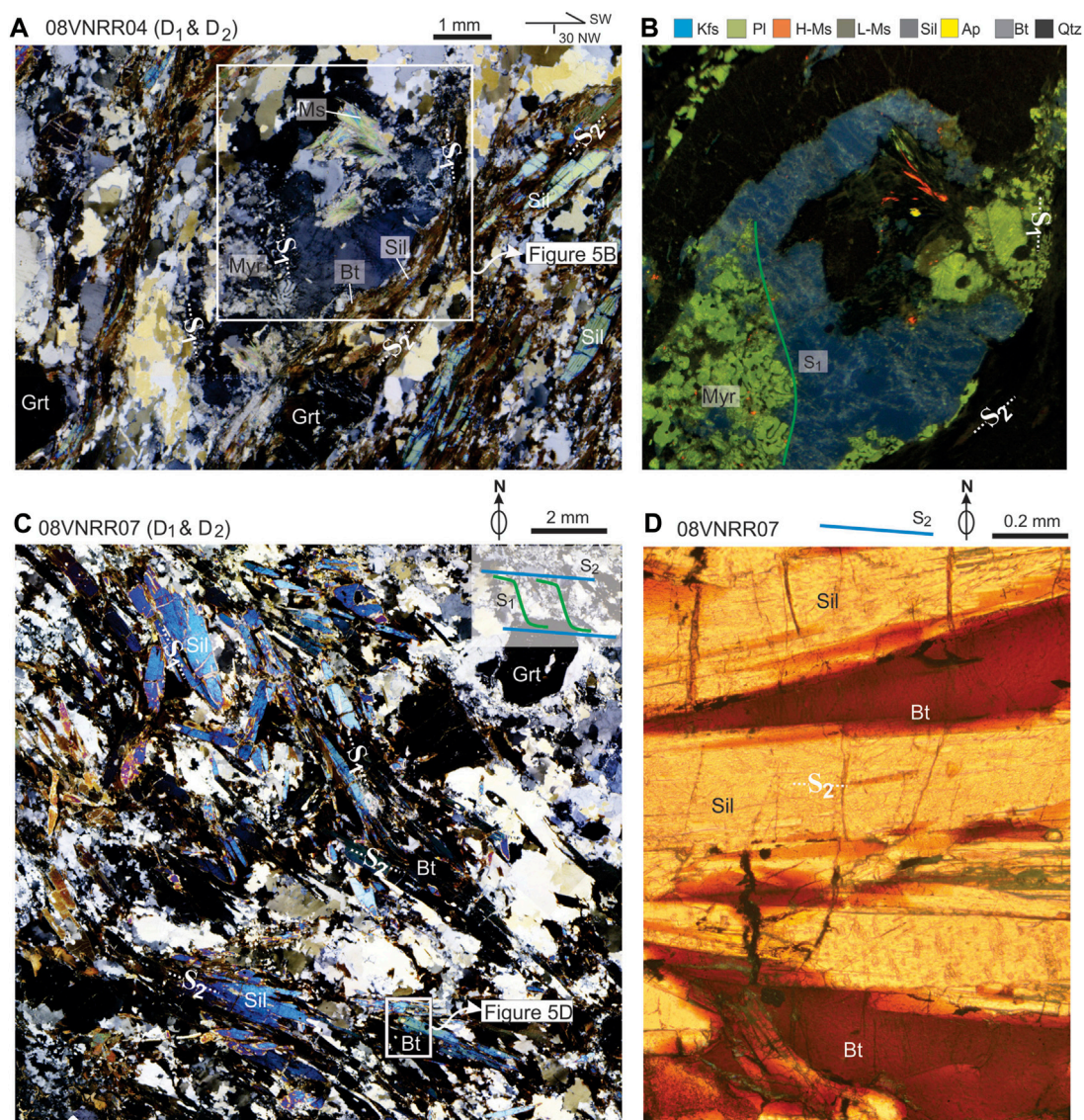
FIGURE 5
Microphotographs and cathodoluminescence (CL) images illustrate the microstructural and petrological relationship of D_1 and D_2 deformation events. **(A)** The XZ plane of sample 08VNRR04 striking SW and dipping towards NW at 30° shows quartz + feldspar + myrmekite aggregated microlithon domain and biotite + sillimanite aligned cleavage domain showing the cross-cutting relationship of S_1 and S_2 foliations. All garnets are rounded and truncated by S_1 and S_2 indicating a pre-to-syn- D_1 deformation event. **(B)** CL image shows that myrmekite extensively developed at the boundary of K-feldspar parallel to S_1 foliation. The blue color represents K-feldspar, and the green represents plagioclase and myrmekite. **(C)** Horizontal thin section of sample 08VNRR07 pointing to the top presents a cross-cutting relationship between S_1 and S_2 foliations. Both S_1 and S_2 are defined by plagioclase, K-feldspar, biotite, quartz, and sillimanite. **(D)** The straight boundary between sillimanite and biotite parallel to S_2 foliation indicates the syn-tectonic growth of sillimanite during the D_2 event. Abbreviations: Bt-biotite; Kfs- K-feldspar; Pl-plagioclase; Grt-garnet; Ms-muscovite; H-Ms- high temperature muscovite; L-Ms- low temperature muscovite Qtz-quartz; Sil-sillimanite; Ap-apatite; Myr-myrmekite.

deformation event happened between upper to lower amphibolite facies (500°C–650°C) condition.

4.1.3 D_3 deformation event

The latest ductile deformation event, D_3, formed the kilometer scale open to tight antiformal dome structure across the DNCV (Figure 2B). The orientation of D_3 fabrics is shown in Figure 3. The poles of folded S_2 foliations are marked by blue circles, whereas the purple circles mark the pole of NW-SE striking NE steep dipping S_3 fold axial planar cleavages. The purple triangles mark the mineral stretching lineation that is parallel to the long axis (NW-SE) of the DNCV massif (Figure 3A). Mylonite zones are strongly developed along both limbs of the DNCV metamorphic massif with dominant left-lateral shear sense indicators including asymmetrical pressure shadows around feldspar augen (Figure 4D), as well as mylonitic S-C fabrics with mica-fishes (Figures 4A, 6B). The orientation of the C plane of the mylonitic S/C fabrics was parallel to the S_3 fold axial plane, and no cross-cutting relationship could be observed between mylonitic fabrics and the D_3 fabrics under both macro and micro scales (Figures 4A, 6C), indicating that the mylonite zones developed
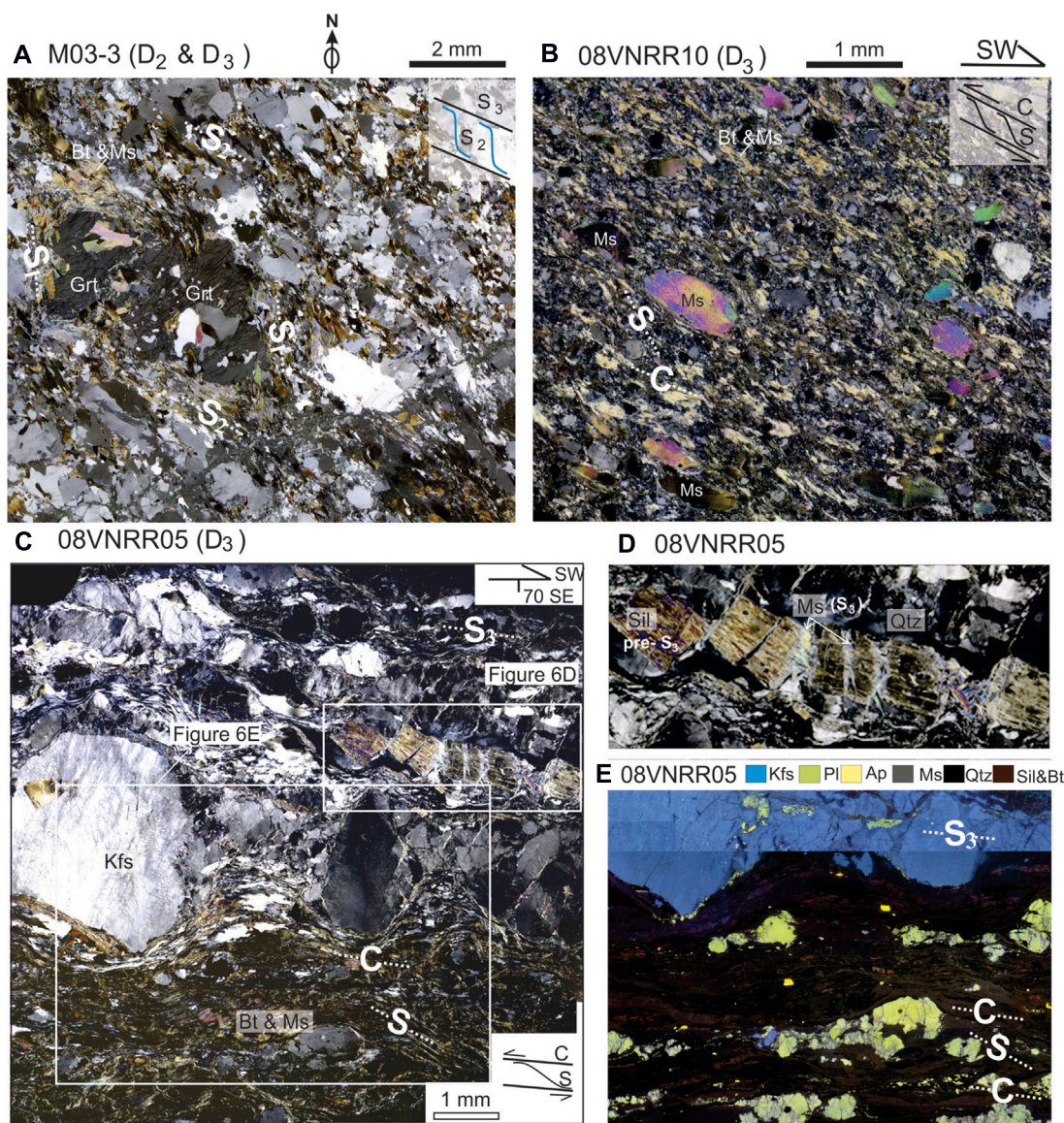
FIGURE 6
Cross-polarized and cathodoluminescence (CL) microphotographs illustrate the microstructural and petrological relationship of D_2 and D_3 deformation events. **(A)** Horizontal thin section of sample M03-3 with the north pointing to the top showing the cross-cutting relationship of S_2 and S_3 foliations. All garnets are truncated by S_2 foliation defined by the orientation of deformed muscovite and biotite with a left-lateral sense of shear. S_3 foliation is indicated by the elongation of muscovite + biotite+ quartz and feldspar. **(B)** Vertical thin section striking to SW of mylonite sample 08VNRR10 showing S-C fabrics with a left-lateral sense of shear. Muscovite fishes are truncated by C fabrics indicating muscovite fish grew pre-to syn-D_3 event. **(C)** XZ plane of sample 08VNRR05 with SW striking, 70° SE dipping showing coarse-grained feldspar phenocrysts with S-C fabrics with left-lateral shearing indicator. Boudinaged sillimanite also indicated a left-lateral sense of shear. The C- plane is defined by muscovite, biotite, elongated quartz, and feldspar ribbon. The S- plane is defined by oriented muscovite and biotite. **(D)** The enlarged image shows the brittle deformation of sillimanite and infilling of new-growth muscovite in sillimanite fractures. **(E)** CL image showing strain localization likely resulting from different grain sizes and chemical reactions. While, in the upper part, K-feldspar has a large grain size with brittle deformation, the lower part mostly presents recrystallization and ductile deformation of fine-grained plagioclase. Abbreviations: Bt-biotite; Kfs- K-feldspar; Pl-plagioclase; Grt-garnet; Ms-muscovite; Qtz-quartz; Sil-sillimanite; Ap-apatite.

contemporaneously with the D_3 doming event. Compared to the core regions that are mainly composed of gneiss and amphibolite interlayers, the mylonite regions have much finer grain size and narrower microlithon domains than the cleavage domain (Figure 4) and strongly developed C fabrics. The shearing fabric (S) was defined by the alignment of coarse-grained muscovite fish and feldspar augens, and fine-grained sillimanite, biotite, plagioclase,

K-feldspar, and quartz aggregates. The shear band cleavage (C) was defined by the alignment of fine-grained muscovite and biotite (Figures 4, 6B). As stated above, muscovite was rarely observed for garnet sillimanite-bearing gneiss. On the contrary, muscovite was an abundant mineral commonly observed within mylonite.

The previously described high-grade mineral assemblages that include orthoclase, garnet, and sillimanite were relics from the D_1
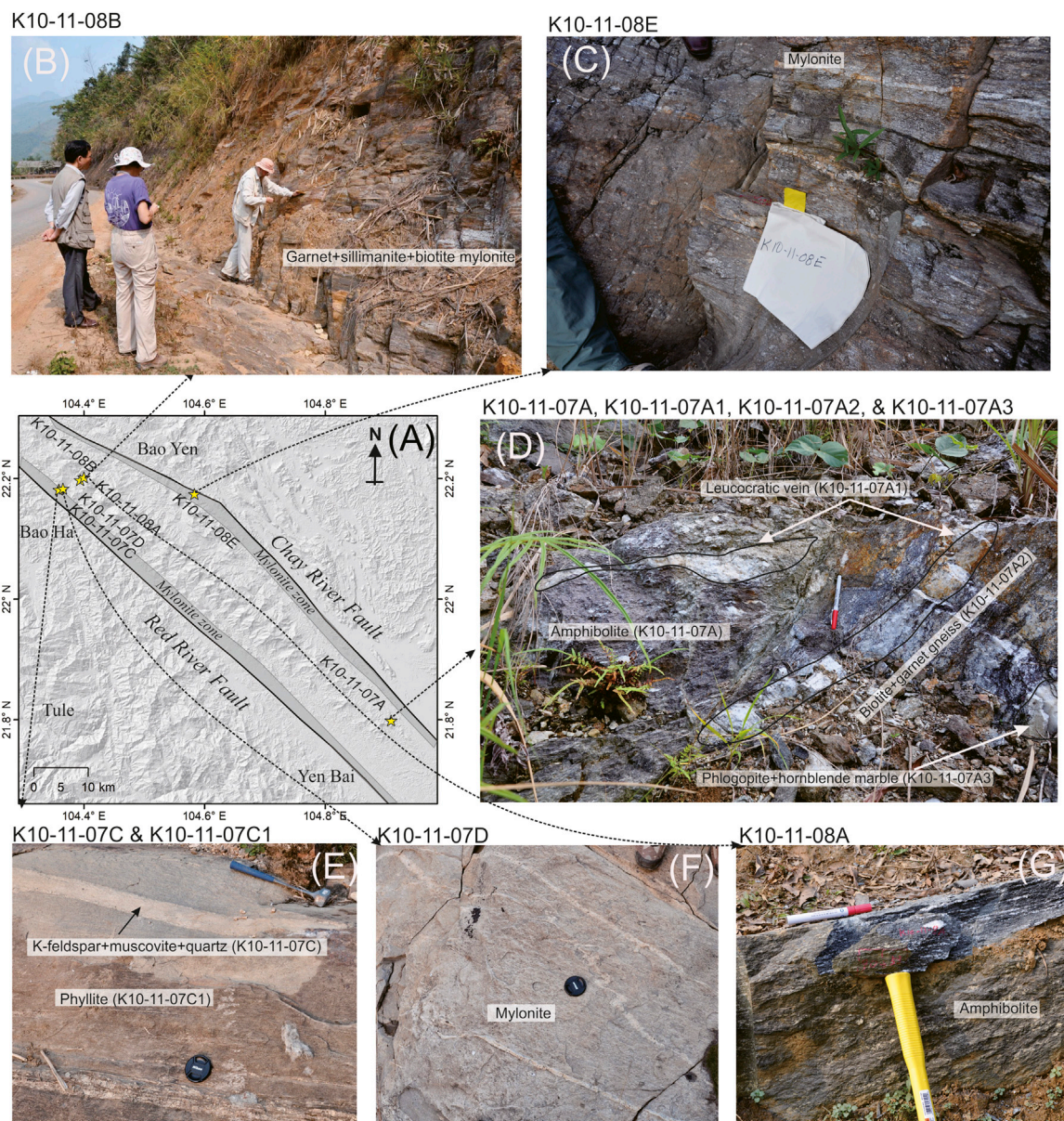
FIGURE 7
(A) Shaded relief map and the field photos showing sample locations for ^{40}Ar-^{39}Ar analysis. **(B)** Sample K10-11-08B showing minerals of garnet, sillimanite, biotite in mylonite, was collected in the inner part of the DNCV metamorphic massif. **(C)** Sample K10-11-08E was separated from the mylonite zone in the eastern portion of the DNCV metamorphic massif. **(D)** Sample K10-11-07A located in the inner part of the DNCV metamorphic massif shows different structural domains and rock types with amphibolite (K10-11-07A), leucocratic vein (K10-11-07A1), gneiss (K10-11-07A2), and marble (K10-11-07A3). **(E)** K-feldspar vein (K10-11-07C) and phyllite (K10-11-07C1) were separated in almost the same location near the rims of the DNCV metamorphic massif. **(F)** Sample K-10-11-07D was separated from the mylonite zone in the western portion of the DNCV metamorphic massif. **(G)** Sample K10-11-08A was collected in the amphibolite in the inner core of the DNCV metamorphic massif. More detail about dating results have been shown in Figure 8 and Table 1.

and D_2 that did not grow during the D_3. They all showed clear evidence of brittle fracturing and/or boudinage (Figure 6C, E) in an orientation consistent with D_3 deformation. The neck of sillimanite boudinage was filled with quartz and muscovite with a basal plane parallel to the direction of extension. This further indicated the syn-D_3 growth of muscovite and the brittle deformation condition of high-grade minerals. The cathodoluminescence microphoto

(Figure 6E) of a mylonitic sample showed a relict K-feldspar porphyroclast, but a near absence of K-feldspar in the finer-grained and well-foliated muscovite-rich domain. This microstructural pattern suggests that the following retrograde metamorphic reaction was likely responsible for foliation development and microtextural softening of the rock during deformation:

FIGURE 8
^{40}Ar-^{39}Ar step heating age spectra of **(A)** amphibole; **(B–E)** muscovite; **(F,G,I)** biotite; **(H)** phlogopite; and **(J–N)** K-feldspars separated from the DNCV metamorphic massif.

$3K$-feldspar $+ 2H+ + \rightarrow$ Muscovite $+ 6SiO2 + 2K+$
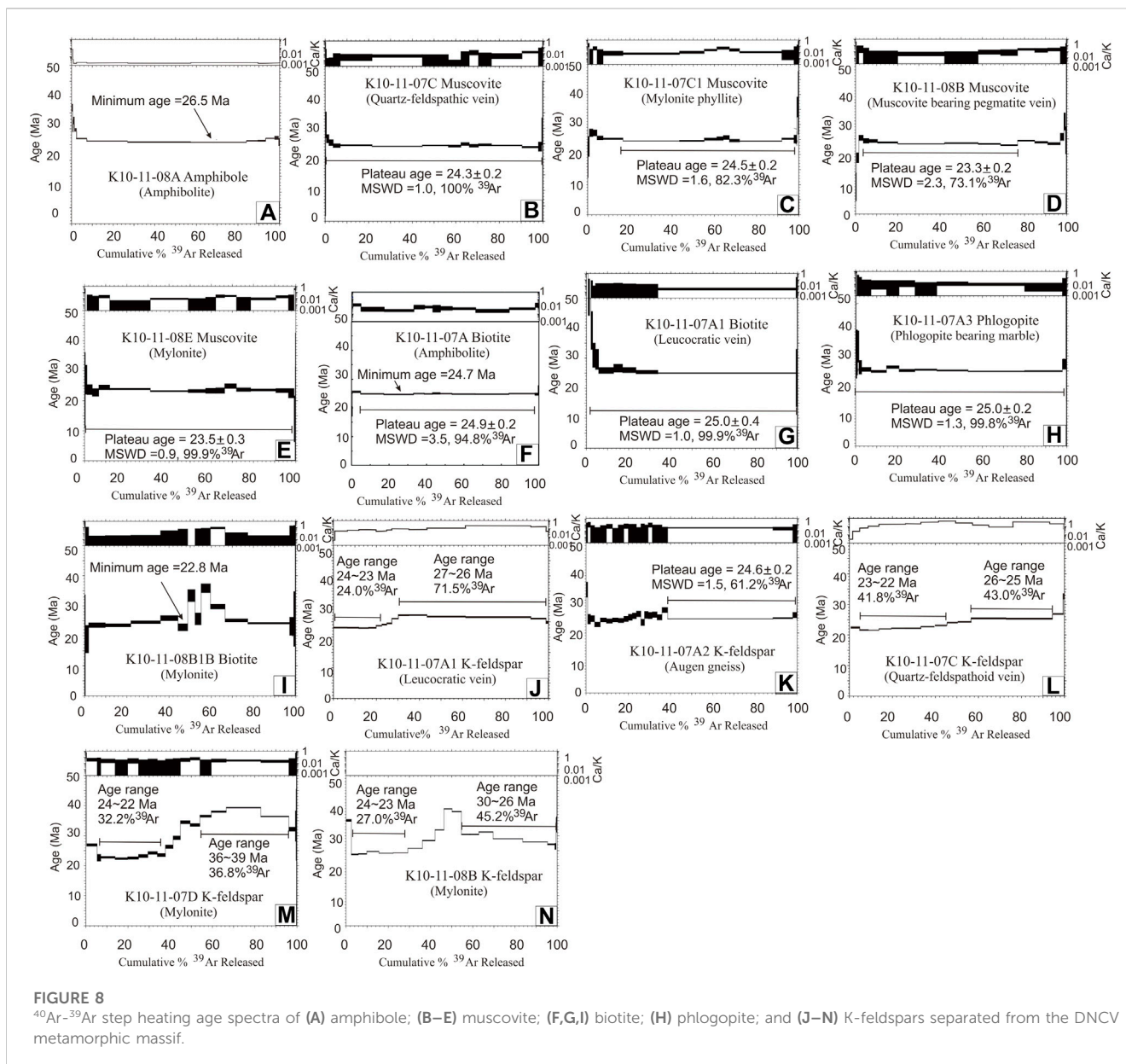
This coexistence of biotite in textural equilibrium with muscovite in the S_3 foliation indicates that the D_3 event occurred above the biotite isograd (400°C; Spear et al., 1999). The brittle fracture of sillimanite and plagioclase within the muscovite-rich domain (Figures 6D, E) suggests the left-lateral shearing of the RRSZ continued from the greenschist facies conditions (400°C–500°C) until brittle deformation condition.

4.2 ^{40}Ar/^{39}Ar geochronology results

As described above, the DNCV metamorphic massif is composed of numerous rock types that went through at least three stages of ductile deformations including prograde granulite facies metamorphism (D_1) and retrograde greenschist facies deformation

associated with left-lateral motion (D_3). Of these, the timing of the D_3 event is most relevant to motion on the RRSZ, tectonic escape, and opening of the SCS. Therefore, in order to constrain the relevant post-peak-metamorphism history of the DNCV metamorphic massif, ^{40}Ar/^{39}Ar step-heating experiments were performed on 14 mineral separates (one amphibole, four muscovites, three biotite, one phlogopite, and five K-feldspars) from different structural and lithological domains across the DNCV metamorphic massif. There was one amphibole separate from the amphibolite interlayer sample (K10-11-08A) that preserved D_2 structures from the core region of the DNCV metamorphic massif (Figure 7), as well as four muscovite separates from the two mylonitic zones (eastern mylonite: K10-11-08E; western mylonitic phyllite: K10-11-07C1, and quartz-feldspathic vein: K10-11-07C) and the high strain belt within the core region (Sil + Bt + Gt gneiss: K10-11-08B; Figure 7). In addition, there were three biotite separates from the north and south outcrops within the core

TABLE 2 Estimated bulk closure temperatures for Amphibole, Phlogopite, Muscovite, Biotite, and K-feldspar with an assumed diffusion dimension of 100 μm for assumed cooling rate from 50 ˚C/Ma to 100˚C/Ma (Schaen et al. (2020)).

Assumed cooling rate (˚C/ Ma)	Tc Amphibole (˚C) Spherical	Tc Phlogopite (˚C) Cylindrical	Tc Muscovite (˚C) Spherical	Tc Biotite (˚C) Cylindrical	Tc K-feldspar (Orthoclase) (˚C) Spherical
Do m²/s	2.40E-06	7.50E-05	2.00E-03	1.50E-06	9.80E-07
E (kJ)	268	242	264	186	183
A	55	27	55	27	55
50	539	417	416	339	299
60	543	420	418	342	302
70	546	422	421	344	304
80	549	424	423	346	306
90	551	426	424	347	308
100	553	428	426	349	309

region of the DNCV metamorphic massif (Figure 7). K10-11-08B1B came from the same Sil + Bt + Gt gneiss K10-11-08B outcrop with muscovite, K10-11-07A and K10-11-07A1 came from the amphibolite and leucogranite vein within the same outcrop. The one phlogopite separate came from the marble layer of the same outcrop (K10-11-07A3) as well. Five K-feldspar separates (K10-11-07A1, K10-11-07A2, K10-11-07C, K10-11-07D, and K10-11-08B) from different rock types were collected from five outcrops with different structural domains across the DNVC metamorphic massif (Table 1; Figure 7). Argon isotopic data and K/Ca vs. cumulative % ^{40}Ar plots are presented graphically in Figure 8, and preferred ages are reported for each sample in Tables 1, 3–7. Complete isotopic data for each step-heating experiment can be found in Supplementary Appendix S5 and in the associated data released by Dinh et al. (2023). In this study, calculated values for the closure temperature of the dated minerals used the Arrhenius parameters summarized by Schaen et al. (2020). Estimated closure temperatures for amphibole, phlogopite, muscovite, biotite, and K-feldspar (orthoclase) are presented in Table 2 In this table, all closure temperatures were calculated by using an assumed diffusion domain size of 100 μm and a rapid cooling rate of 50˚C/Ma to 100˚C/Ma consistent with age data.

4.2.1 Amphibole

Amphibole was separated from an amphibolite interlayer (K10-11-08A) in the core region of the DNCV metamorphic massif (Figure 7). The amphibolite layer was composed of dominantly amphibole and plagioclase and preserved D$_2$ structures. Amphibole grains were optically unzoned and appeared unaltered. A step-heating experiment on an aliquot of amphibole yielded a relatively flat age spectrum and a preferred age of 26.6± 0.1 Ma. The purity of the mineral separate was confirmed by the uniform Ca/K ratios.

4.2.2 Muscovite

Four samples were collected for ^{40}Ar/^{39}Ar analysis of muscovite. These samples came from the DNCV core as well as the east and west-bounding D$_3$ shear zones (Figure 7). Sample K10-11-08B was from a muscovite-bearing pegmatitic vein in the core of the DNCV and near the dated amphibolite sample K10-11-08A. The vein

crosscut a D$_2$ Grt+Sil+Bt gneiss but was deformed, indicating it was a late D$_2$ pegmatite. The sample yielded a plateau age of 23.3 ± 0.2 Ma. Sample K10-11-08E was a mylonitic phyllite from the eastern D$_3$ mylonite zone. The dominant foliation was defined by muscovite fish + quartz and plagioclase aggregates. Muscovite separated from this sample yielded a plateau age of 23.5 ± 0.3 Ma. Samples K10-11-07C and K10-11-07C1 were from the same outcrop within the western D$_3$ mylonitic zone. K10-11-07C1 was a mylonitic phyllite with a dominant foliation defined by muscovite fish + quartz and plagioclase aggregates. Sample K10-11-07C was from a Ksp + Qz+ Ms vein that crosscut the phyllite at a low angle (Figure 7E), suggesting that this vein was syn-S3. These two samples yielded nearly identical plateau ages of 24.3 ± 0.2 Ma and 24.5 ± 0.2 Ma.

4.2.3 Biotite and phlogopite

Three samples were collected for ^{40}Ar/^{39}Ar analysis of biotite and one sample for phlogopite. All four samples were from the core of the DNCV where D$_3$ deformation was limited. Three samples came from the same outcrop in the southeastern portion of the DNCV metamorphic massif. Here biotite+garnet gneiss, amphibolite, and phlogopite marble were interlayered and folded forming F2 folds. Leucocratic veins were also present and were parallel to S2 (Figure 7D). Biotite was separated from both the amphibolite (K10-11-07A), the leucocratic vein (K10-11-07A1), and phlogopite was separated from the marble (K10-11-07A3). The three samples yielded plateau ages of 24.9 ± 0.2 Ma, 25.0 ± 0.4 Ma, and 25.0 ± 0.2 Ma, respectively, and were in general agreement. The fourth sample, K10-11-08B1B, was from farther north, but was also situated within the central portion of the DNCV, and again preserved sub-horizontal S$_2$ fabrics (Figure 7). The sample was a D$_2$ mylonite with an S$_2$ foliation defined by Sil+Bt and garnet also present in the assemblage. The sample yielded a disturbed age spectrum with several anomalously old age steps at approximately 50% of the ^{39}Ar release. However, most of the spectrum yielded ages between 22.8 and 25.6 Ma and a total gas age of 25.4 Ma, in agreement with the other data. The cause(s) of the older age steps in this sample was unknown. No chloritization of biotite was observed in the thin section or the

separated biotite grains, so we suggested the presence of minor excess argon and that 25.4 Ma was the maximum age of the sample.

4.2.4 K-feldspar

Five samples were collected for $^{40}Ar/^{39}Ar$ analysis of K-feldspar. Samples K10-11-07A1 and K10-11-07A2 were from the core in the southern part of the DNCV metamorphic massif. Sample K10-11-07A1 was an S_2-parallel leucocratic vein and sample K10-11-07A2 was a biotite+ K-feldspar +garnet. Sample K10-11-07A1 yielded a climbing age spectrum with low-temperature steps yielding an age of ~23 Ma and high-temperature steps yielding an age of ~26.5 Ma. K10-11-07A2 yielded a similar spectrum with low-temperature steps yielding an age of ~24 Ma and high-temperature steps yielding a plateau age of 24.6 ± 0.2 Ma. Sample K10-11-08B was from the core of the northern portion of the DNCV and samples K10-11-07C and K10-11-07D were from the western margin of the DNCV (Table 1; Figure 7). Sample K10-11-08B was a mylonite and yielded a hump shape spectrum with low-temperature steps yielding an age of ~24 Ma, intermediate-heating steps yielding an age of ~38 Ma, and high-temperature steps yielding an age of ~28 Ma. Sample K10-11-07C was from a quartz-feldspathoid vein located within the D_3 western mylonite zone and had an S/C mylonitic fabric. The sample yielded a climbing age spectrum with low and high-temperature steps yielding ages of ~22 Ma and 25.5 Ma, respectively. Sample K10-11-07D was from a mylonitic phyllonite from the same outcrop and yielded a climbing age spectrum with low-temperature steps yielding an age of ~22 Ma and high-temperature steps yielding a significantly older age of 39 Ma.

4.3 Interpretation of $^{40}Ar/^{39}Ar$ ages

The $^{40}Ar/^{39}Ar$ method has been widely utilized to reconstruct the cooling history, and to constrain the timing of exhumation in various paths of the RRSZ (Wang et al., 1998; Wang et al., 2000; Leloup et al., 2001). As noted above, the RRSZ is a poly-deformed belt with evidence for deformation and associated metamorphic reaction from granulite to the greenschist facies conditions. Therefore, critical to the interpretation of the isotopic ages is the petrologic and structural context of the dated minerals. The mineralogy and structural relationships for amphibolite sample K10-11-08A indicated the dated amphibole grains grew at upper amphibolite facies conditions (>550°C) during D_2, and published work from samples in the same belt yielded peak temperatures of >600°C (Palin et al., 2013). Therefore, we interpreted the $^{40}Ar/^{39}Ar$ system to record the time of cooling through the closure temperature for the diffusion of argon in amphibole at 26.6± 0.1 Ma. This also provided a minimum age constraint on D_2 deformation that pre-dated D_3 of the DNCV metamorphic massif. Muscovite, biotite, and K-feldspar ages were only slightly younger, suggesting rapid cooling (50–100°C/km) through and following amphibole closure-resulting in an amphibole closure temperature of ~540–550°C (Schaen et al., 2020).

In both the core and marginal shear zones of the DNCV metamorphic massif, the muscovite was retrograde, forming folia that truncated higher-grade assemblages (Figure 6A), and/or replaced minerals from the higher-grade assemblage (Figures 5A,

6C, D). Important for the interpretation of the $^{40}Ar/^{39}Ar$ data was the temperature at which these fabric-forming retrograde reactions occurred. In both sample K10-11-07C1 and sample K10-11-08E, the mylonitic D_3 foliation was defined by muscovite and biotite in apparent textural equilibrium. This indicated deformation occurred above the biotite isograd (~400°C) and the brittle fracture of both sillimanite (Figure 6D) and feldspars (Figure 6C) during D_3 suggested a temperature of < ~500°C for D_3 (e.g., Fossen, 2016). In other words, D_3 occurred at ~400–500°C. The calculated closure temperature for muscovite was ~415–425°C, and so we interpreted the similar plateau ages of all samples (24.5-23.3 Ma, Tables 1, 3–7) as cooling ages. These ages could also be growth ages, but due to the rapid cooling rate of the samples, in either interpretation, the geologic conclusions are very similar. These data either constrain the timing of the upper greenschist facies D_3 deformation and mylonite formation to 26.6-23.3 Ma or directly date the growth of mylonite-defining fabrics at 24.5–23.3 Ma.

All biotite (five biotite and one phlogopite) samples yielded similar ages of ~25.4-24.9 Ma. For the reasons given above, we interpreted all ages as cooling ages though 340–350°C and 420–430°C, respectively. In general, the biotite ages were expected to be younger than both phlogopite and muscovite ages due to the biotite's lower closure temperature. However, we observed that biotite ages overlapped with phlogopite ages but were slightly older than most muscovite ages. In as much, as the muscovite and biotite samples were not from identical outcrops and were similar in age, we interpreted the older biotite ages to reflect local differences in cooling rate in this complex structural region. We also could not rule out a minor component of excess argon in biotite as is commonly observed (e.g., Kelley, 2002).

The interpretation of the K-feldspar data was somewhat more complicated, as mineralogically and microstructurally K-feldspars are complicated, and no consensus exists in the geochronology community on the interpretation of K-feldspar degassing data (e.g., Harrison and Lovera, 2014; Villa, 2014). In this research, we interpreted the high-temperature step ages of step-heating experiments to reflect the time of cooling through ~300–310°C (Table 2), and the low-temperature steps to reflect the time of cooling through ~250-150°C (Harrison and McDougall, 1982), and/or recrystallization. Three samples, of which two were from the DNCV core (K10-11-07A1 and K10-11-07A2) and one was from a Qz-Ksp-Ms vein (K10-11-07C) in the western shear zone, yielded nearly identical age spectra with low-temperature steps yielding ages of ~24.0-21.5 Ma and high-temperature steps yielding ages of ~27-25 Ma. The high-temperature ages overlapped with the ages of biotite from the same samples. These values were again consistent with rapid cooling through K-feldspar closure-concomitant with D_3 deformation. Two samples from mylonitic rocks yielded different ages. Sample K10-11-08B from a D_3 shear zone yielded a humped-shaped spectrum with "intermediate age maxima," a feature common in K-feldspar from highly deformed rocks but that is poorly understood (Lovera et al., 2002). Interestingly the low and high-temperature steps yielded similar ages to the other three samples—and we suggested they were broadly consistent. Sample K10-11-07D from the western mylonite yielded a low-temperature age of ~22 Ma, but an anomalously high-temperature age of ~39 Ma. We interpreted this older age to reflect local post-D_3-mylonite vertical displacements within the

TABLE 3 $^{40}Ar/^{39}Ar$ dating result of Amphibole, sample K10-11-08A.

Sample No	Mineral dated		Rock type			Longitude		Latitude
K10-11-08A	Amphibole		Amphibolite			104.36749		22.18094
K10-11-8A Amphibole 126KD57			J = 0.004817			wt. = 205.1 mg		
Temperature (°C)	^{39}Ar(% total)	Radiogenic yield (%)	$^{39}Ar_K$ (moles)	$^{40}Ar*/^{39}Ar_K$	Ca/K	Cl/K	Age (Ma)	Error (Ma)
700	0.0	−673.7	9.91E-17	36.355	***	***	295.4	320.9
900	0.1	24.2	3.84E-13	27.134	4.4307	0.2000	224.9	4.2
1,000	0.5	73.6	8.40E-14	4.309	2.2467	0.0044	37.6	0.6
1,050	0.3	67.4	4.83E-14	3.639	5.7372	0.0060	31.8	1.0
1,075	0.5	78.1	8.17E-14	3.837	8.0128	0.0046	33.5	0.6
1,100	1.0	83.8	1.31E-13	3.486	7.9681	0.0033	30.5	0.3
1,125	4.9	92.8	5.42E-13	3.170	7.3964	0.0023	27.7	0.1
1,150	19.7	94.5	2.06E-12	3.075	7.6982	0.0025	26.9	0.1
1,175	30.2	96.6	3.05E-12	3.039	7.8003	0.0025	26.6	0.1
1,200	26.7	98.1	2.65E-12	3.029	7.5529	0.0023	26.5	0.1
1,225	5.4	92.8	5.77E-13	3.081	7.5415	0.0027	27.0	0.1
1,250	3.7	91.2	4.03E-13	3.088	7.9051	0.0028	27.0	0.1
1,275	4.2	93.6	4.57E-13	3.175	7.7519	0.0025	27.8	0.1
1,300	2.0	90.9	2.21E-13	3.197	7.7821	0.0030	28.0	0.3
1,350	0.6	79.9	7.76E-14	3.034	7.6511	0.0040	26.6	0.6
1,450	0.3	53.5	5.44E-14	3.174	7.7160	0.0068	27.8	0.9
1,650	0.1	7.7	4.11E-13	20.109	7.2464	0.2500	169.2	15.3
1,650	0.0	8.1	1.66E-13	36.672	4.0225	0.5000	297.8	25.7
Plateau age= 26.55 ± 0.1 (Ma)							Integrated age= 27.3 (Ma)	

TABLE 4 ^{40}Ar/^{39}Ar dating results of Muscovite.

Muscovite K10-11-07C					
Sample No	Mineral dated	Rock type		Longitude	Latitude
K10-11-07C	Muscovite	K-feldspar vein close to phyllite		104.35962	22.18013
K10-11-07C Muscovite 92KD57		J = 0.004921		wt. = 2.75 mg	

Temperature (°C)	^{39}Ar (% total)	Radiogenic yield (%)	^{39}Ar$_K$ (moles)	^{40}Ar*/^{39}Ar$_K$	Ca/K	Cl/K	Age (Ma)	Error (Ma)
600	0.2	1.6	5.26E-16	1.381	0.317	0.0191	12.4	10.8
700	0.4	38.7	9.80E-16	3.474	−0.060	0.0004	31.0	4.2
800	1.3	70.6	3.05E-15	2.970	−0.037	0.0005	26.6	1.4
850	1.9	59.7	4.42E-15	2.832	−0.024	0.0007	25.3	0.9
900	3.3	59.8	7.89E-15	2.722	−0.006	0.0006	24.4	0.6
950	14.5	74.7	3.45E-14	2.735	0.004	0.0004	24.5	0.2
1,000	23.1	91.6	5.50E-14	2.700	0.005	0.0003	24.2	0.1
1,050	12.0	95.2	2.87E-14	2.727	0.003	0.0003	24.4	0.2
1,100	5.7	89.8	1.36E-14	2.698	−0.008	0.0000	24.1	0.3
1,150	3.8	88.3	9.12E-15	2.781	0.006	0.0002	24.9	0.5
1,200	4.2	87.5	9.95E-15	2.723	0.020	0.0004	24.4	0.5
1,250	5.9	82.6	1.41E-14	2.752	0.003	0.0005	24.6	0.4
1,300	14.1	92.9	3.37E-14	2.723	0.005	0.0003	24.4	0.1
1,350	7.5	93.6	1.80E-14	2.669	0.017	0.0004	23.9	0.3
1,450	1.4	81.4	3.31E-15	2.684	0.040	0.0002	24.0	1.5
1,650	0.4	48.3	9.86E-16	3.236	−0.012	0.0012	28.9	4.4
1,650	0.1	7.4	2.19E-16	1.331	−0.230	0.0066	12.0	20.3
1,650	0.1	4.6	1.32E-16	1.531	−0.111	0.0122	13.7	31.5

| Plateau age= 24.31± 0.18 (Ma) | | | | | | | Integrated age= 24.4 (Ma) | |

Muscovite K10-11-07C1					
Sample No	Mineral dated	Rock type		Longitude	Latitude
K10-11-07C1	Muscovite	Phyllite		104.35962	22.18013
K10-11-07C1 Muscovite 44KD57		J = 0.004819 ± 0.50%			

Temperature (°C)	^{39}Ar (% total)	Radiogenic yield (%)	^{39}Ar$_K$ (moles)	^{40}Ar*/^{39}Ar$_K$	Ca/K	Cl/K	Age (Ma)	Error (Ma)
600	0.3	10.7	6.21E-16	2.032	0.094	0.0109	18.1	5.9
700	0.6	45.6	1.13E-15	2.540	0.161	0.0032	22.6	3.3
800	1.5	78.6	2.81E-15	3.053	−0.005	0.0010	27.2	1.3
850	1.9	82.1	3.53E-15	3.051	0.053	0.0000	27.2	1.0
900	3.0	72.8	5.47E-15	2.855	0.007	0.0003	25.4	0.7
950	9.4	67.7	1.72E-14	2.830	0.009	0.0004	25.2	0.3
1,000	26.6	78.4	4.86E-14	2.744	0.006	0.0003	24.4	0.1
1,050	11.9	91.5	2.17E-14	2.739	0.011	0.0004	24.4	0.2
1,100	5.9	87.2	1.08E-14	2.815	0.024	0.0003	25.1	0.4
1,150	3.0	77.0	5.50E-15	2.836	0.049	0.0004	25.3	0.6

TABLE 4 (*Continued*) $^{40}Ar/^{39}Ar$ dating results of Muscovite.

Muscovite K10-11-07C1

Sample No	Mineral dated		Rock type				Longitude	Latitude
1,200	2.9	76.0	5.38E-15	2.882	0.045	0.0005	25.7	0.7
1,250	4.8	60.0	8.73E-15	2.756	0.024	0.0006	24.6	0.5
1,300	20.0	85.9	3.64E-14	2.742	0.010	0.0003	24.4	0.1
1,350	5.7	92.9	1.04E-14	2.831	0.011	0.0005	25.2	0.3
1,450	1.4	72.6	2.55E-15	2.819	0.036	0.0001	25.1	1.3
1,650	0.6	38.6	1.06E-15	4.025	0.060	0.0007	35.7	3.4
1,650	0.2	8.8	3.81E-16	4.187	0.331	0.0041	37.2	10.5
1,650	0.1	10.4	1.45E-16	9.328	−0.076	−0.0062	81.8	27.0

Plateau age= 24.5 ± 0.2   Integrated age= 24.9 (Ma)

Muscovite K10-11-08B

Sample No	Mineral dated	Rock type	Longitude	Latitude
K10-11-08B	Muscovite	Pegmatitic feldspar vein with muscovite	104.39417	22.19635
K10-11-08B Muscovite 100KD57		J = 0.004916± 0.50%	wt. = 2.98 mg	

Temperature (°C)	^{39}Ar (% total)	Radiogenic yield (%)	$^{39}Ar_K$ (moles)	$^{40}Ar*/^{39}Ar_k$	Ca/K	Cl/K	Age (Ma)	Error (Ma)
600	0.5	2.6	1.32E-15	0.990	0.251	0.0124	8.9	4.6
700	1.2	38.1	2.80E-15	2.084	0.018	0.0020	18.7	1.7
800	2.1	64.1	5.14E-15	2.831	0.041	0.0016	25.3	0.9
850	2.6	78.3	6.20E-15	2.715	0.006	0.0007	24.3	0.8
900	4.0	77.8	9.68E-15	2.715	−0.006	0.0006	24.3	0.5
950	9.7	77.9	2.34E-14	2.656	0.005	0.0009	23.7	0.2
1,000	22.1	92.1	5.33E-14	2.601	0.005	0.0009	23.3	0.1
1,050	15.9	96.0	3.84E-14	2.631	0.004	0.0010	23.5	0.1
1,100	10.6	91.8	2.54E-14	2.600	0.010	0.0011	23.2	0.2
1,150	8.1	86.5	1.96E-14	2.558	0.011	0.0015	22.9	0.2
1,200	8.1	90.7	1.94E-14	2.720	0.023	0.0014	24.3	0.2
1,250	6.2	86.4	1.49E-14	2.664	0.019	0.0009	23.8	0.4
1,300	6.0	88.6	1.44E-14	2.609	0.023	0.0008	23.3	0.4
1,350	1.6	88.8	3.93E-15	2.866	0.009	0.0008	25.6	1.2
1,450	0.7	90.6	1.70E-15	3.438	−0.055	−0.0008	30.7	2.9
1,650	0.5	36.9	1.14E-15	2.738	0.056	0.0007	24.5	4.5
1,650	0.1	4.6	1.32E-16	4.081	0.571	0.0207	36.4	38.3
1,650	0.0	6.2	7.10E-17	7.896	0.453	−0.0291	69.7	70.8

Plateau age= 23.3± 0.2 (Ma)   Integrated age= 23.5 (Ma)

Muscovite K10-11-08E

Sample No	Mineral dated	Rock type	Longitude	Latitude
K10-11-08E	Muscovite	Mylonite	104.58536	22.17402
K10-11-08E Muscovite 102KD57		J = 0.004889 ± 0.50%	wt. = 2.79 mg	

TABLE 4 (*Continued*) ^{40}Ar/^{39}Ar dating results of Muscovite.

Temperature (°C)	^{39}Ar (% total)	Radiogenic Yield (%)	^{39}Ar$_k$ (moles)	^{40}Ar*/^{39}Ar$_k$	Ca/K	Cl/K	Age (Ma)	Error (Ma)
600	0.4	3.1	9.13E-16	2.643	0.209	0.0116	23.5	12.6
700	0.9	37.4	1.98E-15	3.036	−0.060	0.0009	27.0	4.9
800	2.5	66.1	5.61E-15	2.659	0.019	0.0004	23.6	1.7
850	3.2	63.9	7.26E-15	2.550	0.007	0.0002	22.7	1.3
900	5.2	59.8	1.18E-14	2.742	0.021	0.0002	24.4	0.8
950	19.1	71.5	4.36E-14	2.687	0.001	0.0001	23.9	0.2
1,000	17.9	88.1	4.09E-14	2.595	0.008	0.0002	23.1	0.2
1,050	8.3	83.5	1.90E-14	2.604	0.003	0.0002	23.2	0.5
1,100	4.8	76.3	1.09E-14	2.616	0.003	0.0004	23.3	0.9
1,150	4.2	73.5	9.68E-15	2.627	0.023	0.0003	23.4	1.0
1,200	5.6	48.6	1.28E-14	2.791	0.025	0.0004	24.8	0.8
1,250	6.6	61.7	1.52E-14	2.661	0.007	0.0003	23.7	0.6
1,300	12.0	81.1	2.73E-14	2.644	0.009	0.0003	23.5	0.3
1,350	6.0	81.4	1.37E-14	2.619	0.019	0.0002	23.3	0.7
1,450	2.6	59.1	6.00E-15	2.523	0.016	0.0000	22.4	1.5
1,650	0.5	13.5	1.21E-15	1.565	0.317	0.0017	13.9	7.7
1,650	0.1	−12.4	1.78E-16	−2.323	0.782	0.0021	−20.9	52.2
1,650	0.0	−21.8	9.76E-17	−6.064	−1.713	−0.0045	−55.1	97.6
Plateau age= 23.5± 0.3 (Ma)						Integrated age= 23.4 (Ma)		

western mylonite zone. In this scenario, sample K10-11-07D was in the lower greenschist facies (~250–300°C) during incipient D$_3$ deformation at ~25 Ma. This resulted in the recrystallization of some feldspar during D$_3$ (22 Ma) but also the preservation of relict (pre-D$_3$) ^{40}Ar in K-feldspar porphyroclast.

4.4 Reconstructed cooling path and timing structural events of the DNCV

Based on our structural, petrological, and geochronological data, and the interpretations aforementioned we reconstructed a cooling path for the DNCV metamorphic massif (Figure 9). All phlogopite, muscovite, and biotite ages were interpreted as cooling ages (see above) and were plotted with ±25°C error bars on the closure temperatures reported in Table 2. K-feldspar high-temperature steps ages were plotted with a closure temperature of ~300–310°C and the low-temperature step ages were plotted at ~250–150°C, recognizing that recrystallization also played a role in the argon systematics. Three different cooling paths were reconstructed for different lithology units as they went through different paths. For the amphibolite and garnet-biotite-sillimanite gneiss within the core of the DNCV dome, the timing and peak temperature conditions could be linked via our new amphibole, phlogopite, muscovite, biotite, and K-feldspar ages within the core region. The amphibole cooling ages reported by Wang et al. (1998) and

the timing of peak metamorphism from Palin et al. (2013) were also combined with our reconstructed cooling path (dashed green line in Figure 9B). The thermal evolution of the core of the DNCV dropped from 700°C to 550°C around 32 Ma, but remained within 540°C–550°C from 32 Ma until 26 Ma. The core further uplifted to 410°C–430°C condition during 26–24 Ma followed by further uplifting till ~200°C condition during 23 Ma. Similarly, by combining all muscovite and K-feldspar ages within the mylonite zones, a steep cooling path from 410 to 430°C condition starting from 24 Ma until ~200°C condition during 22 Ma was indicated (gray solid line in Figure 9B). Although we did not collect any samples from the deformed Eocene leucogranite bodies, we reconstructed a third cooling path for these magmatic units based on previously reported ages (Harrison et al., 1996; Leloup et al., 2001; Palin et al., 2013). We observed a rapid cooling path from 800°C to 350°C around 34 Ma followed by stable conditions of 350°C to 300°C between 34 and 24 Ma followed by a rapid cooling to ~200°C condition during 22 Ma (red dash line in Figure 9B).

The timing of D$_1$ to D$_3$ corresponded to the reconstructed cooling paths that were allocated according to the estimated metamorphic conditions and observed structural styles. As our petrography and structural results indicated, the D$_1$ occurred under granulite facies with compressional conditions. Therefore, we linked the timing of D$_1$ to before 32 Ma but after the youngest magmatism that intruded the DNCV (35 Ma; Zhang and Schärer, 1999). Although the Permian-Triassic Indosinian orogeny is the most dominant magmatic

TABLE 5 ⁴⁰Ar/³⁹Ar dating result of Biotite.

Biotite K10-11-07A				
Sample No	Mineral dated	Rock type	Longitude	Latitude
K10-11-07A	Biotite	Amphibolite	104.91108	21.79692
K10-11-07A Biotite 73KD57		J = 0.004845 ± 0.5 %	wt. = 18.3 mg	

Temperature (°C)	^{39}Ar (% total)	Radiogenic yield (%)	^{39}Ar$_K$ (moles)	^{40}Ar*/^{39}Ar$_K$	Ca/K	Cl/K	Age (Ma)	Error (Ma)
600	0.1	5.5	2.68E-15	6.245	0.9910	0.1429	55.5	2.4
700	0.4	30.4	8.90E-15	2.094	0.2084	0.0132	18.8	0.9
800	4.4	56.4	1.13E-13	2.857	0.0190	0.0087	25.6	0.1
850	12.4	85.4	3.21E-13	2.779	0.0055	0.0068	24.9	0.1
900	15.9	95.1	4.09E-13	2.752	0.0033	0.0065	24.7	0.1
950	5.7	95.1	1.47E-13	2.791	0.0107	0.0071	25.0	0.1
1,000	4.4	95.8	1.13E-13	2.776	0.0097	0.0065	24.9	0.1
1,050	4.1	95.7	1.05E-13	2.796	0.0087	0.0066	25.0	0.1
1,100	6.3	95.6	1.63E-13	2.787	0.0072	0.0063	25.0	0.1
1,150	12.5	95.0	3.21E-13	2.767	0.0058	0.0064	24.8	0.1
1,200	17.9	95.2	4.62E-13	2.764	0.0031	0.0065	24.8	0.1
1,250	13.9	95.6	3.58E-13	2.788	0.0057	0.0065	25.0	0.1
1,300	1.7	88.5	4.46E-14	2.763	0.0206	0.0066	24.8	0.2
1,350	0.3	75.8	8.83E-15	2.944	0.0809	0.0081	26.4	0.7
1,450	0.0	19.7	4.51E-16	4.414	0.5231	0.0263	39.4	11.6
1,650	0.0	11.5	4.53E-16	5.673	0.0685	0.0769	50.5	10.6
1,650	0.0	9.5	1.02E-16	16.101	2.4795	0.2000	139.7	60.7

No plateau age	Integrated age = 24.9 (Ma)

Biotite K10-11-07A1				
Sample No	Mineral dated	Rock type	Longitude	Latitude
K10-11-07A1	Biotite	Leucocratic dyke	104.91108	21.79692
K10-11-07A1 Biotite 28KD59		J = 0.009363 ± 0.0000468	wt. = 0.5 mg	

TABLE 5 (*Continued*) ^{40}Ar/^{39}Ar dating result of Biotite.

Temperature (°C)	^{39}Ar (% total)	Radiogenic yield (%)	^{39}Ar$_K$ (moles)	^{40}Ar*/^{39}Ar$_K$	Ca/K	Cl/K	Age (Ma)	Error (Ma)
600	0.2	2.0	6.34E-16	2.249	1.8822	0.1142	38.1	45.2
700	0.2	38.7	6.10E-16	7.542	1.6513	0.2070	124.6	32.6
850	0.6	51.5	2.32E-15	4.509	0.9254	0.1128	75.5	9.0
900	0.6	69.8	2.32E-15	3.121	−0.0051	0.0158	52.6	8.5
925	0.6	122.9	2.19E-15	3.946	−0.1774	0.0078	66.3	9.0
950	0.8	85.0	3.18E-15	2.311	−0.0339	0.0070	39.1	6.4
975	1.3	74.7	4.90E-15	1.822	−0.0538	0.0051	30.9	4.1
1,000	1.6	72.4	6.25E-15	1.741	−0.0279	0.0048	29.5	3.3
1,100	7.1	45.5	2.68E-14	1.519	0.0119	0.0093	25.8	1.0
1,150	4.3	80.4	1.63E-14	1.565	0.0082	0.0181	26.6	1.3
1,200	6.3	78.9	2.40E-14	1.530	0.0075	0.0181	26.0	0.9
1,250	10.4	71.6	3.93E-14	1.487	0.0078	0.0111	25.3	0.6
1,350	65.4	89.7	2.48E-13	1.466	0.0030	0.0467	24.9	0.1
1,450	0.6	34.7	2.14E-15	1.369	0.0981	0.4174	23.3	9.6
1,650	0.1	11.3	1.99E-16	5.747	−0.7250	0.6764	95.7	103.0
1,650	0.0	9.0	1.43E-17	50.917	11.7876	0.1244	712.3	1,000.3

Plateau age = 25.0 ± 0.4 (Ma)							Integrated age = 26.4 Ma	

Biotite K10-11-08B1B								

Sample No	Mineral dated		Rock type			Longitude		Latitude
K10-11-08B1B	Biotite		Garnet + sillimanite + biotite + mylonite			104.39417		22.19635
K10-11-8B1B Biotite 88KD57			J = 0.004841 ± 0.0000242			wt. = 0.93 mg		

Temperature (°C)	^{39}Ar (% total)	Radiogenic yield (%)	^{39}Ar$_K$ (moles)	^{40}Ar*/^{39}Ar$_K$	Ca/K	Cl/K	Age (Ma)	Error (Ma)
600	0.5	0.9	3.36E-16	1.607	0.485	0.0247	14.4	19.1
700	1.5	24.2	1.02E-15	2.110	−0.027	0.0055	18.9	4.6
800	7.9	68.6	5.32E-15	2.625	−0.020	0.0077	23.5	0.8

(Continued on following page)

TABLE 5 (*Continued*) ⁴⁰Ar/³⁹Ar dating result of Biotite.

Biotite K10-11-08B1B								
Sample No	Mineral dated		Rock type			Longitude		Latitude
850	12.3	88.6	8.27E-15	2.624	−0.011	0.0081	23.5	0.5
900	13.9	95.4	9.39E-15	2.736	−0.010	0.0082	24.5	0.5
950	8.3	98.7	5.62E-15	2.885	0.001	0.0080	25.8	0.9
1,000	4.6	84.4	3.09E-15	2.542	−0.004	0.0082	22.8	1.3
1,050	3.4	111.2	2.26E-15	3.730	−0.130	0.0072	33.3	2.0
1,100	2.9	81.7	1.98E-15	2.851	−0.007	0.0080	25.5	2.0
1,150	4.5	92.8	3.01E-15	4.011	−0.003	0.0098	35.8	1.5
1,200	7.0	93.5	4.69E-15	3.320	0.076	0.0084	29.7	0.9
1,250	10.7	76.1	7.24E-15	2.802	−0.005	0.0083	25.1	0.6
1,300	19.7	92.3	1.33E-14	2.695	−0.005	0.0078	24.1	0.3
1,350	2.0	68.8	1.33E-15	2.581	0.078	0.0066	23.1	3.0
1,450	0.6	54.9	4.33E-16	2.858	−0.102	0.0082	25.6	9.2
1,650	0.1	13.6	4.58E-17	11.909	−1.639	0.0252	104.3	81.5
1,650	0.0	8.8	2.30E-17	10.576	−1.489	−0.0008	92.9	160.2
1,650	0.0	−4.3	2.27E-17	−4.543	7.483	0.0483	−41.4	178.8
No plateau age							Integrated age = 25.4 Ma	

TABLE 6 ^{40}Ar/^{39}Ar dating result of Phlogopite.

Phlogopite K10-11-07A3								
Sample No	Mineral dated		Rock type			Longitude		Latitude
K10-11-07A3	Phlogopite		Marble + amphibole+ phlogopite			104.91108		21.79692
K10-11-07A3 Phlogopite 46KD57			J = 0.004904± 0.50 %			wt.= 2.6 mg		
Temperature (°C)	^{39}Ar (% total)	Radiogenic yield (%)	^{39}Ar$_K$ (moles)	^{40}Ar*/^{39}Ar$_K$	Ca/K	Cl/K	Age (Ma)	Error (Ma)
600	0.2	−0.1	3.75E-16	−0.126	0.456	0.0327	−1.1	23.2
700	0.2	27.2	4.82E-16	5.158	0.433	0.0029	45.7	14.9
800	0.4	44.6	8.82E-16	3.429	0.755	0.0010	30.5	8.0
850	0.4	64.2	9.26E-16	3.494	−0.023	0.0015	31.1	7.5
900	0.6	60.4	1.32E-15	3.716	0.050	0.0013	33.0	5.2
950	1.3	57.0	3.03E-15	2.933	0.029	0.0017	26.1	2.3
1,000	4.4	60.7	1.04E-14	2.857	0.021	0.0011	25.5	0.7
1,050	7.3	78.6	1.72E-14	2.777	0.015	0.0012	24.8	0.4
1,100	5.9	93.6	1.39E-14	2.940	0.015	0.0009	26.2	0.5
1,150	7.4	89.6	1.75E-14	2.814	0.017	0.0012	25.1	0.4
1,200	10.6	74.4	2.48E-14	2.844	0.005	0.0012	25.4	0.3
1,250	14.6	74.2	3.45E-14	2.822	0.011	0.0011	25.2	0.2
1,300	26.8	87.8	6.30E-14	2.787	0.008	0.0011	24.8	0.1
1,350	17.8	91.8	4.20E-14	2.792	0.006	0.0010	24.9	0.2
1,450	1.7	77.7	4.10E-15	3.046	0.014	0.0008	27.1	1.7
1,650	0.2	27.6	5.86E-16	4.829	0.008	0.0024	42.8	12.1
1,650	0.1	31.5	1.71E-16	6.188	−0.117	0.0017	54.7	39.8
1,650	0.0	15.7	6.26E-17	6.284	0.385	−0.0226	55.5	109.6
Plateau Age = 25 ± 0.2 (Ma)							Integrated age= 25.3 (Ma)	

TABLE 7 $^{40}Ar/^{39}Ar$ dating results of K-feldspar.

K-feldspar K10-11-07A1								
Sample No	Mineral dated		Rock type			Longitude		Latitude
K10-11-07A1	K-feldspar		Leucocratic dyke			104.91108		21.79692
K10-11-07A1 K-feldspar 107KD57			J = 0.004806 ± 0.5 %			wt. = 27.9 mg		
Temperature (°C)	^{39}Ar (% total)	Radiogenic yield (%)	$^{39}Ar_K$ (moles)	$^{40}Ar*/^{39}Ar_K$	Ca/K	Cl/K	Age (Ma)	Error (Ma)
700	0.6	27.8	3.39E-14	11.235	0.2326	0.0345	97.9	6.5
750	5.8	89.2	3.15E-13	2.669	0.0225	0.0003	23.7	0.1
800	5.3	95.0	2.89E-13	2.666	0.0188	0.0002	23.7	0.1
850	4.5	95.2	2.45E-13	2.585	0.0155	***	23.0	0.1
900	3.4	94.9	1.87E-13	2.645	0.0167	0.0002	23.5	0.1
950	2.7	93.4	1.46E-13	2.685	0.0232	0.0002	23.9	0.1
1,000	2.3	89.8	1.23E-13	2.698	0.0215	0.0004	24.0	0.1
1,050	2.4	87.0	1.29E-13	2.788	0.0170	0.0004	24.8	0.1
1,100	3.0	82.1	1.64E-13	2.924	0.0125	0.0007	26.0	0.1
1,150	4.9	77.9	2.65E-13	3.065	0.0133	0.0009	27.2	0.1
1,200	8.4	81.2	4.56E-13	3.063	0.0145	0.0008	27.2	0.1
1,250	17.8	85.9	9.68E-13	2.995	0.0107	0.0005	26.6	0.1
1,300	30.3	87.6	1.64E-12	2.965	0.0057	0.0004	26.3	0.1
1,350	7.1	87.1	3.86E-13	2.909	0.0071	0.0006	25.9	0.1
1,400	1.1	86.5	5.81E-14	2.832	0.0232	0.0007	25.2	0.2
1,450	0.3	82.5	1.34E-14	2.921	0.0897	0.0012	26.0	0.9
1,650	0.2	60.7	9.44E-15	2.765	0.0159	0.0029	24.6	0.9
1,650	0.0	7.2	9.97E-17	8.226	5.2743	0.1667	72.2	80.1
No Plateau age						Integrated age= 26.2 (Ma)		

K-feldspar K10-11-07A2								
Sample No	Mineral dated		Rock type			Longitude		Latitude
K10-11-07A2	K-Feldspar		Biotite+Garnet+ augen Feldspar			104.91108		21.79692
K10-11-07A2 K-feldspar 30KD57			J = 0.00478 ± 0.50%			wt. = 2.8 mg		
Temperature (°C)	^{39}Ar (% total)	Radiogenic yield (%)	$^{39}Ar_K$ (moles)	$^{40}Ar*/^{39}Ar_k$	Ca/K	Cl/K	Age (Ma)	Error (Ma)
600	0.2	25.0	4.60E-16	10.374	−0.388	0.0153	90.0	13.6
700	0.8	63.5	2.44E-15	3.901	0.021	0.0020	34.4	2.5
750	1.2	91.9	3.55E-15	2.778	0.135	0.0005	24.5	1.7
800	2.0	97.7	6.04E-15	2.802	0.013	0.0004	24.8	1.0
850	2.6	90.9	7.88E-15	2.573	−0.018	0.0006	22.7	0.8
900	2.9	97.1	8.70E-15	2.743	0.032	0.0005	24.2	0.7
950	3.0	95.8	8.85E-15	2.705	0.061	0.0001	23.9	0.7
1,000	2.8	88.9	8.32E-15	2.743	−0.017	0.0004	24.2	0.7
1,050	2.5	86.6	7.60E-15	2.724	0.035	0.0005	24.1	0.8
1,100	2.1	92.0	6.44E-15	2.788	0.073	0.0004	24.6	0.9
1,150	1.9	93.2	5.68E-15	2.844	0.044	0.0006	25.1	1.0
1,200	2.1	92.4	6.17E-15	2.900	0.044	0.0005	25.6	0.9
1,250	2.1	95.2	6.28E-15	2.978	−0.021	0.0005	26.3	0.9

TABLE 7 (*Continued*) ^{40}Ar/^{39}Ar dating results of K-feldspar.

K-feldspar K10-11-07A2

Sample No	Mineral dated		Rock type			Longitude		Latitude
1,275	1.7	87.5	5.20E-15	2.656	0.057	0.0004	23.5	1.1
1,300	1.7	92.0	5.11E-15	2.937	0.016	0.0004	25.9	1.1
1,325	2.0	86.5	5.86E-15	2.917	0.097	0.0002	25.8	1.1
1,350	2.2	86.6	6.67E-15	2.942	0.030	0.0007	26.0	1.0
1,375	2.4	86.2	7.21E-15	2.847	0.030	0.0004	25.1	0.9
1,400	2.6	66.6	7.84E-15	3.127	−0.009	0.0000	27.6	0.9
1,450	49.9	86.8	1.50E-13	2.783	0.027	0.0003	24.6	0.1
1,550	9.4	87.5	2.83E-14	2.814	0.025	0.0002	24.9	0.2
1,650	1.9	77.4	5.77E-15	2.933	0.038	0.0008	25.9	1.0

Plateau Age = 24.6 ± 0.2	Integrated age= 25 (Ma)

K-feldspar K10-11-07C

Sample No	Mineral dated		Rock type			Longitude		Latitude
K10-11-07C	K-feldspar		K-feldspar vein close to phyllite			104.35962		22.18013
K10-11-07C K-feldspar 97KD57			J = 0.004831± 0.5 %			wt. = 27.26 mg		

Temperature (°C)	^{39}Ar(% total)	Radiogenic yield (%)	^{39}Ar$_K$ (moles)	^{40}Ar*/^{39}Ar$_K$	Ca/K	Cl/K	Age (Ma)	Error (Ma)
700	0.7	16.5	2.06E-14	11.619	0.3206	0.0667	101.6	1.1
750	4.8	69.8	1.39E-13	2.494	0.0357	0.0013	22.3	0.1
800	4.1	83.5	1.20E-13	2.398	0.0386	0.0007	21.5	0.1
850	4.1	87.9	1.20E-13	2.409	0.0353	0.0005	21.5	0.1
900	4.8	90.7	1.38E-13	2.454	0.0266	0.0002	22.0	0.1
950	5.7	92.0	1.66E-13	2.514	0.0259	0.0002	22.5	0.1
1,000	6.2	90.7	1.79E-13	2.514	0.0266	0.0003	22.5	0.1
1,050	6.2	91.1	1.79E-13	2.564	0.0212	0.0002	22.9	0.1
1,100	6.0	88.9	1.74E-13	2.612	0.0187	0.0003	23.4	0.1
1,150	6.3	80.6	1.83E-13	2.686	0.0184	0.0006	24.0	0.1
1,200	7.4	71.8	2.14E-13	2.738	0.0215	0.0011	24.5	0.1
1,250	16.6	65.4	4.84E-13	2.842	0.0284	0.0017	25.4	0.1
1,300	21.8	69.8	6.35E-13	2.863	0.0135	0.0014	25.6	0.1
1,350	3.6	68.2	1.06E-13	2.892	0.0174	0.0017	25.8	0.1
1,400	1.4	62.5	3.97E-14	3.023	0.0364	0.0025	27.0	0.3
1,450	0.4	58.9	1.06E-14	3.054	0.0370	0.0029	27.3	0.9
1,650	0.1	33.6	2.51E-15	3.702	0.1850	0.0112	33.0	4.3
1,650	0.0	11.9	6.16E-17	25.328	5.0327	0.2500	214.7	118.0

No Plateau age	Integrated age= 24.6 (Ma)

K-feldspar K10-11-07D

Sample No	Mineral dated		Rock type			Longitude		Latitude
K10-11-07D	K-feldspar		Muscovite mylonite			104.35852		22.17977
K10-11-07D K-feldspars 28KD57			J = 0.004778 ± 0.50%			wt.= 2.8 mg		

Temperature (°C)	^{39}Ar (% total)	Radiogenic Yield (%)	^{39}Ar$_K$ (moles)	^{40}Ar*/^{39}Ar$_k$	Ca/K	Cl/K	Age (Ma)	Error (Ma)
600	0.5	37.7	1.42E-15	13.931	0.305	0.0094	119.9	4.5
700	5.0	89.0	1.38E-14	3.035	0.045	0.0004	26.8	0.4

TABLE 7 (*Continued*) $^{40}Ar/^{39}Ar$ dating results of K-feldspar.

K-feldspar K10-11-07D

Sample No	Mineral dated		Rock type			Longitude		Latitude
750	1.8	95.2	4.85E-15	2.559	0.003	0.0003	22.6	1.2
800	6.8	96.4	1.89E-14	2.566	0.029	0.0004	22.7	0.3
850	5.8	96.1	1.60E-14	2.524	0.013	0.0003	22.3	0.4
900	5.2	89.7	1.45E-14	2.544	0.034	0.0002	22.5	0.4
950	4.5	94.3	1.25E-14	2.623	0.009	0.0004	23.2	0.5
1,000	4.2	98.0	1.17E-14	2.738	0.017	0.0005	24.2	0.5
1,050	3.9	92.7	1.08E-14	2.658	−0.006	0.0004	23.5	0.5
1,100	3.6	95.2	9.95E-15	2.967	0.015	0.0003	26.2	0.6
1,150	3.5	91.4	9.74E-15	3.312	0.020	0.0006	29.2	0.6
1,200	4.6	75.2	1.26E-14	3.906	0.045	0.0007	34.4	0.5
1,250	4.7	83.1	1.31E-14	3.806	0.060	0.0006	33.5	0.4
1,275	5.3	89.7	1.47E-14	4.131	0.013	0.0005	36.4	0.4
1,300	7.1	93.7	1.96E-14	4.312	0.032	0.0005	37.9	0.3
1,325	16.4	95.4	4.53E-14	4.461	0.029	0.0006	39.2	0.1
1,350	13.3	96.0	3.69E-14	4.122	0.022	0.0006	36.3	0.2
1,375	2.9	93.8	8.14E-15	3.643	0.018	0.0007	32.1	0.7
1,400	0.4	74.5	1.12E-15	3.761	0.168	0.0019	33.1	5.1
1,450	0.2	44.7	4.77E-16	3.811	0.074	0.0007	33.6	11.8
1,550	0.1	51.9	3.85E-16	6.602	0.185	−0.0004	57.8	14.9
1,650	0.0	11.1	8.97E-17	4.795	5.170	0.0312	42.1	67.5
No Plateau age							Integrated age= 31.6 (Ma)	

K-feldspar K10-11-08B

Sample No	Mineral dated	Rock type	Longitude	Latitude
K10-11-08B	K-feldspar	Pegmatic feldspar vein with muscovite	104.39417	22.19635

K10-11-08B K-feldspars 104KD57				J = 0.004807 ± 0.50%				
Temperature (℃)	^{39}Ar (%total)	Radiogenic yield (%)	$^{39}Ar_k$ (moles)	$^{40}Ar*/^{39}Ar_k$	Ca/K	Cl/K	Age (Ma)	Error (Ma)
600	0.2	86.4	1.32E-15	70.896	0	0.0031	544.6	5.3
700	2.5	90.4	1.92E-14	3.947	0	−0.0001	35.0	0.3
750	3.2	96.9	2.43E-14	2.661	0	−0.0001	23.7	0.2
800	4.2	99.0	3.25E-14	2.682	0	0.0000	23.8	0.1
850	5.7	99.4	4.37E-14	2.775	0	0.0001	24.7	0.1
900	6.8	97.1	5.17E-14	2.704	0	0.0000	24.0	0.1
950	7.2	98.8	5.47E-14	2.722	0	0.0000	24.2	0.1
1,000	6.9	99.2	5.27E-14	2.892	0	0.0000	25.7	0.1
1,050	6.1	99.0	4.64E-14	3.193	0	−0.0001	28.3	0.1
1,100	4.4	98.9	3.35E-14	3.584	0	0.0000	31.8	0.1
1,150	3.8	97.0	2.94E-14	4.388	0	0.0000	38.9	0.2
1,200	4.5	89.2	3.41E-14	4.282	0	0.0000	37.9	0.2
1,250	4.0	89.9	3.10E-14	3.419	0	0.0000	30.3	0.2
1,275	4.3	91.4	3.31E-14	3.420	0	−0.0001	30.3	0.2

TABLE 7 (*Continued*) ^{40}Ar/^{39}Ar dating results of K-feldspar.

K-feldspar K10-11-08B								
Sample No	Mineral dated		Rock type			Longitude		Latitude
1,300	6.7	93.6	5.11E-14	3.513	0	0.0000	31.2	0.2
1,325	14.2	92.4	1.09E-13	3.255	0	0.0000	28.9	0.1
1,350	12.0	91.3	9.19E-14	3.138	0	0.0000	27.9	0.1
1,375	3.4	90.2	2.63E-14	3.039	0	−0.0001	27.0	0.2
1,400	0.5	84.7	3.93E-15	2.970	0	−0.0006	26.4	1.0
1,450	0.3	103.0	2.25E-15	3.841	0	0.0001	34.0	1.9
1,550	0.2	74.4	1.61E-15	3.790	0	−0.0002	33.6	2.6
1,650	0.0	32.3	3.68E-16	8.229	0	−0.0046	72.2	11.3
1,650	0.0	28.4	7.00E-17	31.919	0	−0.0056	265.4	61.5
No Plateau age						Integrated age= 29.6 (Ma)		

event that produced the majority of granitic rocks in northern Vietnam (Carter et al., 2001; Usuki et al., 2015; Shellnutt et al., 2020) and provided a more suitable kinematic condition for D$_1$, it is unlikely that the high-grade metamorphic condition remained from the Permian-Triassic time until the Eocene. Without the cross-cutting relationship of granite introducing into the D$_1$ structure nor the D$_1$ structure deforming these Eocene leucogranites, the actual timing of D$_1$ cannot be distinguished and, with our current data, we can only suggest that it occurred before 32 Ma. The stable thermal condition under amphibolite facies between 26 and 32 Ma coincided with the sub-horizontal folding. Hence, we allocated this time period to D$_2$ with an estimated cooling rate of ~25°C/Ma. The retrograde evolution from amphibolite facies to the greenschist facies between 26–22 Ma was considered to be the timing of D$_3$, with an estimated cooling rate of ~100°C/Ma. The timing of shear belt development was defined between 24 and 22 Ma as the cooling path for mylonitic rocks. Brittle deformation occurred after 22 Ma, with an estimated cooling rate of ~10°C/Ma, which is similar to the static denudation (≤10°C/Ma; Costa et al., 1993). If we convert the cooling rate to rock exhumation rate by assuming an average continental geotherm of 25°C/km (Criss, 2020), D$_2$ uplifted the DNCV metamorphic massif from 30-28 km to 20-18 km with an uplifting rate of 1.2 mm/year, and D$_3$ uplifted the DNCV massif from ~20 km to ~8 km with an uplifting rate of 3 mm/year. The uplifting rate of 1–3 mm/year was not fast compared to the average uplifting rate of orogenic belts, which is 4–10 mm/year. Instead, it nearly fell within the average denudation rate of ca 2–5 mm/year for the tropical regions for the time scale over tens of million years (Regard et al., 2016). Therefore, the cooling path that we reconstructed was a feasible one, and the "rapid cooling" could correspond to the D$_3$ up-right doming accompanied by tropical fast denudation rather than to the strike-slip shearing-induced uplifting.

5 Discussion

5.1 Comparison of ^{40}Ar/^{39}Ar data with previous works

The ^{40}Ar/^{39}Ar system can be a thermochronometer and/or a geochronometer. In a poly-deformed geologic setting, and/or a setting where deformation and mineral growth continue over a wide temperature range, it is possible that multiple age groups from the same phase can be obtained. We also plotted previously reported ^{40}Ar/^{39}Ar ages (Harrison et al., 1996; Wang et al., 1998; Leloup et al., 2001) in Figure 9. Our results were broadly consistent with Wang et al. (1998) as nearly all data points fell along the reconstructed cooling curve. Harrison et al. (1996) and Leloup et al. (2001) showed quite different results (older and wider age ranges) that were unlikely compatible with our proposed cooling path. Due to the strain partitioning, the structure preserved within different portions of the DNCV metamorphic massif was heterogeneous. However, that did not greatly vary the ages of the same mineral that passes through the closure temperature, and the youngest age of the same mineral separates marked the timing for passing through the closure age. No distinct variation for the cooling pattern was noticed between the north outcrop *versus* the southern outcrop within the DNCV. The granitic rocks further away from the DNCV massif might have contributed to the wider age range reported by Leloup et al. (2001). Searle et al. (2006) pointed out that these granitic rocks were formed pre-shearing, and had nothing to do with left-lateral shearing along the RRSZ. Hence, the ^{40}Ar/^{39}Ar ages obtained from these granitic rocks may not provide timing for shearing. All our samples were collected within different structural domains including the mylonite belts along the DNCV massif, making a more reliable reconstruction of the geochronological-thermal evolution.

5.2 Newly constrained timing of left lateral shearing along the RRSZ

Multiple structural events within the DNCV metamorphic massif were reported by numerous studies (e.g., Ankczkiewicz et al., 2007; Yeh et al., 2008). Different interpretations have been given to explain what type of deformation event is syn-shearing. Our petrological and structural reconstruction indicated three ductile deformation events. The granulite facies to upper amphibolite facies centimeter to meter scale NNW-SSE striking upright D$_1$ folds formed prior to 32 Ma. This D$_1$ event can be linked to the peak metamorphism as previously published studies noted (e.g., Nam et al., 1998; Gilley et al., 2003; Khoi et al., 2016). Wang and Burchfiel
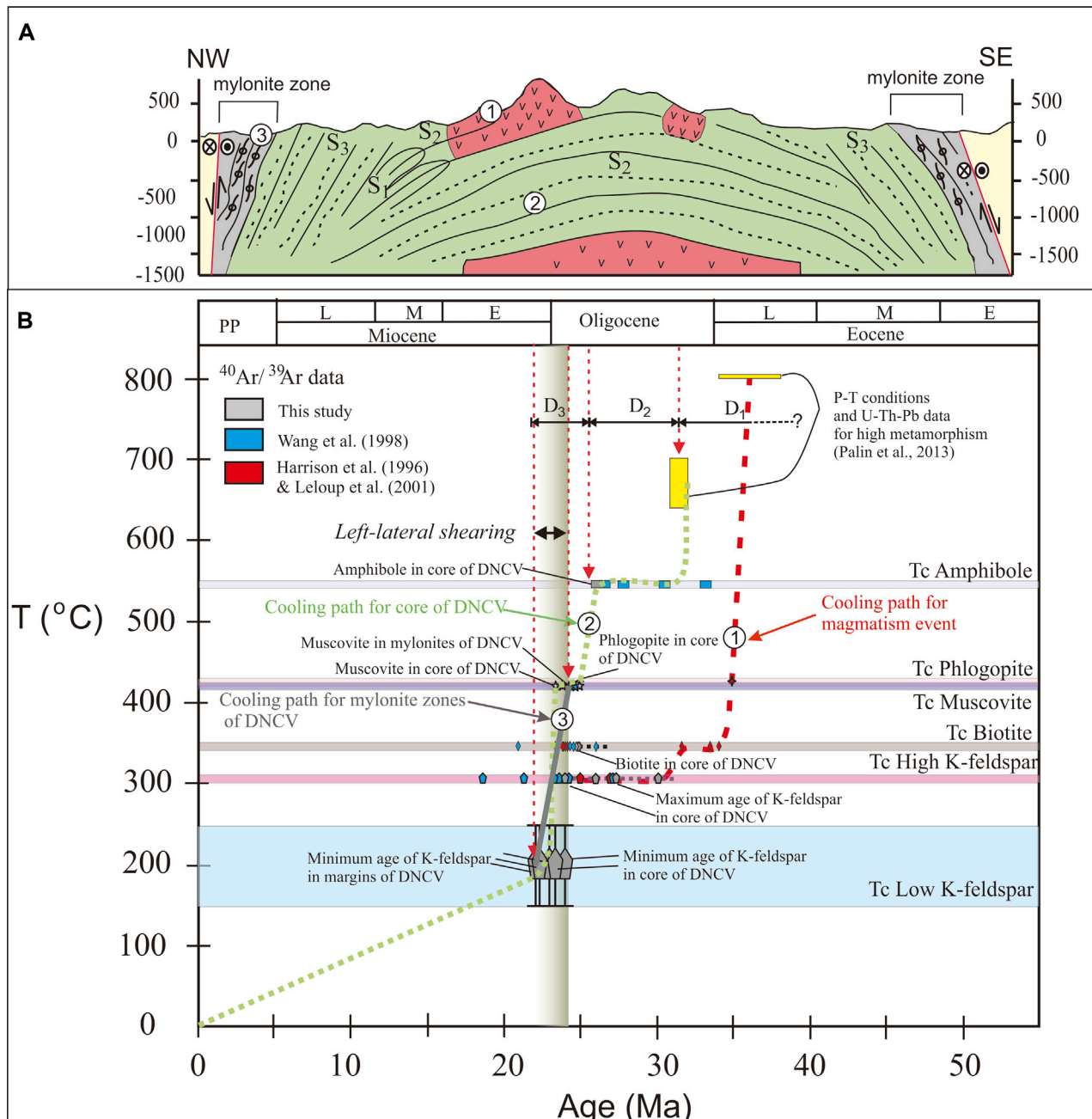
FIGURE 9
Reconstructed cooling paths of different lithological units within the Day Nui Con Voi metamorphic massif based on our age results and published data (Harrison et al., 1996; Wang et al., 1998; Leloup et al., 2001; Palin et al., 2013). **(A)** Cross section indicating the three lithological units that are used for cooling path reconstruction. The green region represents the metamorphic complex core, and the red region represents the Eocene leucogranites that are deformed by D_2. The gray region represents the mylonitic belts. **(B)** The reconstructed cooling paths of the Eocene leucogranite rocks (red dashed line), metamorphic complex core (green dashed line), and mylonitic belts (gray solid line). The yellow box represents data from Palin et al. (2013) for high-temperature deformation of the DNCV metamorphic massif. Rectangle, 4-branch star, 5-branch star, and rhombus indicate $^{40}Ar/^{39}Ar$ data of amphibole, phlogopite, muscovite, and biotite, respectively. Pentagon and pentagon with bar represent high- and low-temperature K-feldspar, respectively. The estimated closure temperatures of different minerals are Tc of amphibole: ~540–550°C; Tc of phlogopite: ~420–430°C; Tc of muscovite: ~415–425°C; Tc of biotite: ~340–350°C; Tc of High K-feldspar (orthoclase): ~300–310°C (Table 2); and Tc of Low K-feldspar: ~150–250°C (Harrison and McDougall, 1982).

(1997) and Jolivet et al. (2001) suggested crustal thickening with regional shortening structures that occurred in southeastern China and northern Vietnam result from the India and Eurasia collision during the Eocene to Early Oligocene. The mechanism of crustal

thickening with regional shortening structures is suggested to have caused the lithology units to reach the granulite facies condition and anatexis melting of the over thickened crust. The emplacement of Eocene leucogranite was further supported by Zhang and Scharer (1999).
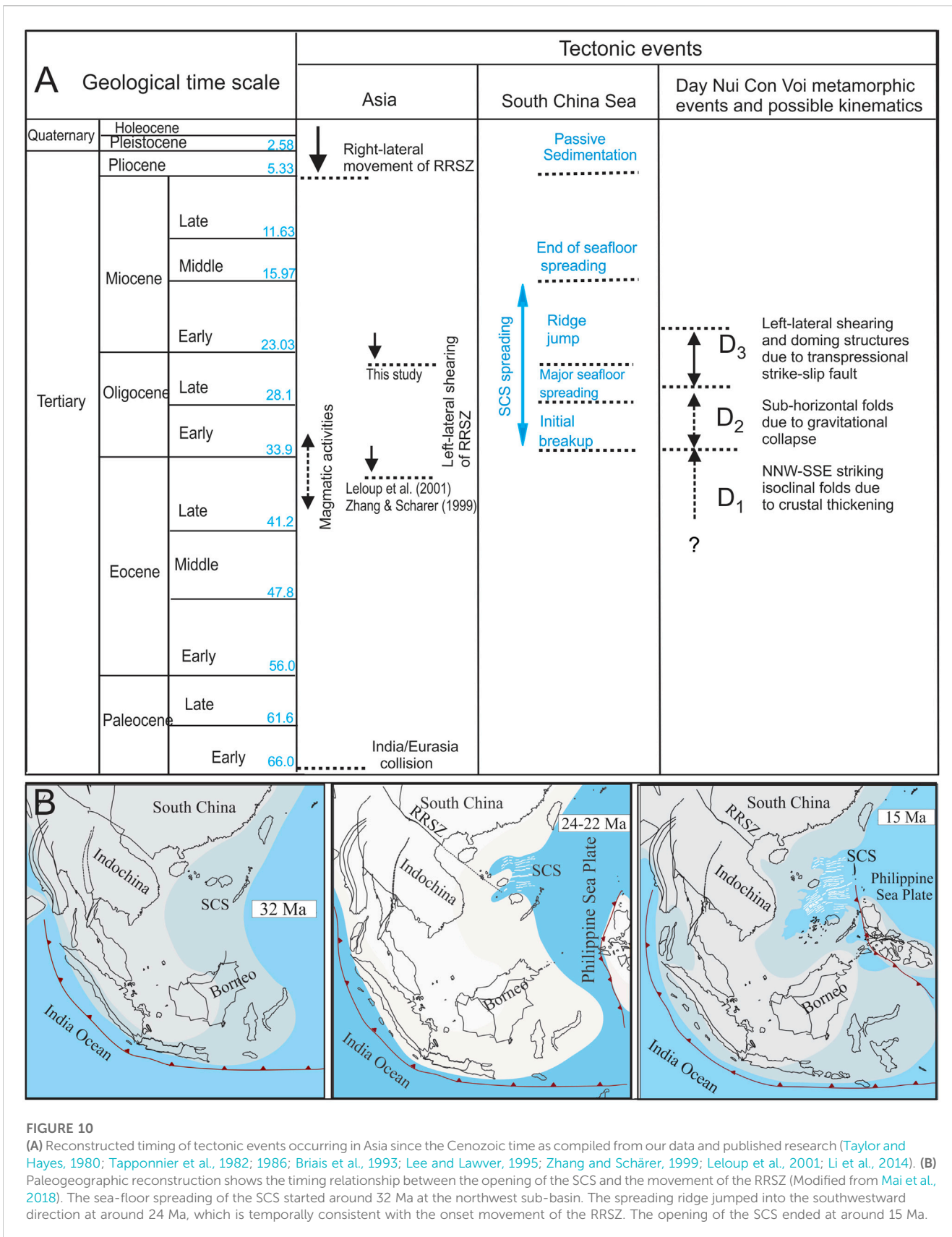
FIGURE 10
(A) Reconstructed timing of tectonic events occurring in Asia since the Cenozoic time as compiled from our data and published research (Taylor and Hayes, 1980; Tapponnier et al., 1982; 1986; Briais et al., 1993; Lee and Lawver, 1995; Zhang and Schärer, 1999; Leloup et al., 2001; Li et al., 2014). **(B)** Paleogeographic reconstruction shows the timing relationship between the opening of the SCS and the movement of the RRSZ (Modified from Mai et al., 2018). The sea-floor spreading of the SCS started around 32 Ma at the northwest sub-basin. The spreading ridge jumped into the southwestward direction at around 24 Ma, which is temporally consistent with the onset movement of the RRSZ. The opening of the SCS ended at around 15 Ma.

The amphibolite facies meter-scale subhorizontal D_2 folds occurred during 32-26 Ma. Similar structures were also observed by Jolivet et al. (2001) in the DNCV metamorphic massif and by Zhang et al. (2021) in the Diancang Shan metamorphic massif. Jolivet et al. (2001) indicated the horizontal structures observed in the DNCV metamorphic massif had been formed due to sub-

horizontal shear doming. Yeh et al. (2008), on the other hand, further explained the subhorizontal shear folding due to gravitational collapsing instead of shear doming. Changing to gravitational collapse after crustal thickening is a common phenomenon in most mountainous regions, such as: in the Alps and Himalaya mountain ranges (Burov, 2010), and in the Fansipan mountain range of northern Vietnam (Dinh et al., 2022). We considered the DNCV metamorphic massif to be no exception, that the thickened crust of the massif started to collapse during D_2. The collapse of the thickened mountain ranges caused the maximum principal stress (σ_1) to change direction from horizontal to vertical, and formed the horizontal folding structures as observed in the D_2 deformation event. The stable thermal condition under amphibolite facies, with little cooling/ up-lifting, is expressed in our reconstructed cooling path. Such stress setting is not suitable for triggering left-lateral shearing event; thus, we do not consider D_2 to be a syn-shearing event.

The D_3 doming event under green schist facies during ~26–22 Ma was considered to be a syn-shearing event. Petrological and microstructural analyses indicated that the D_3 deformation event occurred under greenschist facies conditions with muscovite fish bearing mylonite. The muscovite fish and other shear sense indicators all showed a left-lateral sense of shear. The same orientation of the shear plan of the S/C fabrics and the S_3 fold axial plane indicated that these fabrics were formed under the same deformation event. The temperature ranges of greenschist facies nearly overlapped the closure temperatures in the argon system for amphibole, muscovite, biotite, phlogopite, and K-feldspar (Table 2). This allowed us to provide better constraints on the timing, rate, and duration of the D_3 event. As the closure temperature of the amphibole was consistent with the upper limit of the inferred temperature for the D_3 event, the minimum age of the amphibole (ca. 26 Ma) was used to constrain the onset timing of the D_3 deformation event. The minimum age of K-feldspar (ca. 22 Ma) could be used to provide the termination time of the D_3 event. Although the reconstructed cooling path indicated relatively rapid cooling since 26 Ma, and duration time for the D_3 event of ~26–22 Ma, our microstructural and petrological analyses of mylonite showed syn-shearing growth of muscovite. The cooling ages of muscovite (~24 Ma), thus, was marked as the upper bound of the initiation of the left-lateral shearing activity. The termination of the left-lateral shearing was marked as the mylonites had passed the brittle-ductile transition condition, marked by the youngest age of K-feldspar (~22 Ma). Thus, the timing for left-lateral shearing was further constrained from ~24 Ma to ~22 Ma.

Previous studies linked our D_2 and D_3 together (Jolivet et al., 2001; Anczkiewicz et al., 2007; Viola and Anczkiewicz, 2008) by suggesting a transtensional kinematic condition to form the sub-horizontal folds that were later sheared into a dome via transtension This extensional setting created the space for high-grade metamorphic and magmatic rocks from the lower crustal portion to be uplifted to form the core of the dome. Hence, according to their reconstructed structural evolution, the youngest magmatism within the DNCV (Eocene to Early Oligocene; e.g., Chung et al., 1997) was syn-shearing. Zhang and Schärer (1999) and Leloup et al. (2001) constrained the

timing for the onset of left-lateral shearing along the RRSZ to be around 35 Ma by dating the undeformed granitic rocks from the Fansipan massif, 10 km away from the RRSZ. A wide distribution of undeformed Late Eocene granitic rocks with ages ranging from around 39 to 30 Ma was reported across the Tibetan Plateau, Yunnan, and Vietnam regions (e.g., Chung et al., 1997; Junlai et al., 2020; Gou et al., 2021; Li et al., 2021). This geographical distribution further contradicted the hypothesis that these magmatism events were syn-transtensional shearing. On the contrary, these magmatism events corresponded to our D_1 granulite facies metamorphism as the thickened crust started to stretch and extend. Geochemical data of Chung et al. (1997) and Gou et al. (2021) revealed these magmas originated from collapsing of the thickened crust within plate following the India-Eurasia collision. However, the proposed transtension shearing was not the forming mechanism for our D_3 event as a transtensional basin rather than a dome would have been expected in such a case. We agree with Yeh et al. (2008) that a transpressional condition with sub-horizontal compression along with an oblique component of strike-slip movement further compressed the high-grade metamorphic rocks from the middle crustal level to the upper crystal level. The tectonic transition from the D_2 gravitational collapse to D_3 left-lateral transpressional shearing can be explained by the interaction between tectonics and surface processes. Gravitational collapse likely occurred in the high mountainous area as a result of gravitational potential energy that produced the vertical maximum principle stress (σ_1). After some time, the mountain heights would be reduced due to the effect of surface processes, particularly erosion. Under the intense impact of the erosional process, together with continued crustal shortening in the Indochina block in response to the oblique collision between the India and Eurasia block, the direction of maximum principle stress (σ_1) will switch from vertical to horizontal. In this scenario, the transpressional tectonic setting would likely occur, which could result in the D_3 structures observed in the DNCV metamorphic massif.

5.3 Tectonic implications of the evolution of the DNCV metamorphic massif

Structural styles are fundamentally controlled by regional tectonic settings. Thus, structural changes are a direct reflection of the change in the tectonic setting. Vietnam is situated between the Tibetan plateau and the SCS, which means the structural evolution would be influenced by the Cenozoic India Eurasia collision and the Cenozoic opening of the SCS. The geodynamics of the thickened continental crust within and around the Tibetan Plateau would also affect the structural activities of many oblique regions such as in SE Asia. Following the India-Eurasia collision, the extrusion of the SE Asia continental crust away from India during the Tertiary induced many large-scale strike-slip faults (Tapponnier et al., 1982; tapponnier et al., 1986). Among the strike-slip faults, the RRSZ fault is considered one of the most significant geological structures in SE Asia. Left-lateral strike-slip movement along the RRSZ has been widely regarded as a tectonic mechanism for the opening of the SCS as supported by the indentation extrusion model (Tapponnier et al., 1982; tapponnier et al., 1986). If the indentation

extrusion tectonism is corrected, tectonic events/deformation of the whole process will be in accordance with the time sequence for the opening of SCS as shown in Figure 1A.

Based on data from our study and the published research of others, we have reconstructed the temporal relationship of tectonic events that occurred in Asia (Figure 10). The onset of sea-floor spreading in the SCS was suggested to be around 32 Ma at the northwest sub-basin (Briais et al., 1993; Lee and Lawver, 1995). The ridge jumped southwestward around 24 Ma (Li et al., 2014). The spreading of the SCS ended at around 15 Ma (Taylor and Hayes, 1980; Briais et al., 1993). By assuming the undeformed 39 to 30 Ma granitic rocks as the anatexial product of the syn-shearing activity, this shearing activity was considered to cause the opening of the SCS as the Indochina block extruded (Jolivet et al., 2001; Leloup et al., 2001; Anczkiewicz et al., 2007; Viola and Anczkiewicz, 2008). Our new constrained age of ~24–22 Ma for the shear activity suggested otherwise. The SCS had opened before the initiation of the left-lateral shear activity of the RRSZ. The formation of the protolith of our D_1 gneiss fabrics, which formed under granulite facies prior to 32 Ma, can be linked to crustal thinning due to back arc extension and subduction of Neotethys as the SCS opened (e.g., Karig, 1971; Mai et al., 2018). These granulite facies metamorphism and wide-spread regional leucogranitic magmatism played a critical role in crustal weakening before the strike-slip movement (e.g., Chung et al., 1997; Junlai et al., 2020; Gou et al., 2021; Li et al., 2021). As the SCS further rifted, the continental crust was further thinned. Yeh et al. (2008) reported the sub-horizontal fold (D_2) with the sense of shear of a top to NW and bottom to SW sense of shear along the sub-horizontal folds (D_2). The rapid cooling following the D_2 sub-horizontal folding with retrograde metamorphism reflects this crustal thinning condition. Based on our reconstructed cooling paths of leucogranite and the core of the DNCV, the continental crust of northern Vietnam has been thermally weakened by the Eocene magmatism followed by crustal stretching and thinning due to gravitational collapsing prior to the development of mylonite belts that initiated movement along the RRSZ.

Our interpretation of ~24–22 Ma for the left-lateral movement of the RRSZ matches the southwestward ridge jumping event of the SCS (e.g., Karig, 1971; Mai et al., 2018). Kinematically, it would be difficult for a low-density continental crust to "push" a dense oceanic crust. Therefore, it is unlikely that the left-lateral movement along the RRSZ triggered the southwestward ridge jump in the SCS. On the contrary, the continental crust moved along with the oceanic crust as the ridge jumped. In such a case, a northwestward younging trend should be expected for the initiation age of the RRSZ as the shear activity propagated from the oceanic crust to the continental crust. In other words, if the RRSZ was a result of southeastward extrusion as proposed by the indentation extrusion model (Tapponnier et al., 1982; tapponnier et al., 1986), the shear zone should have developed and propagated from the SW corner of the Tibetan plateau toward the SCS. Initiation age is expected to be older for the northwestern-most metamorphic complex, such that Diancang Shan is older than Ailao Shan that, inturn, is older than the DNCV metamorphic massif. Leloup et al. (2001) showed different cooling histories preserved from different portions of the RRSZ. The reported initiation age within the southeastern part of the Ailao Shan massif was between 21–17 Ma (Harrison et al., 1996; Leloup et al., 2001), and that for the Diancang Shan massif was between 23–17 Ma (Yeh et al., 2014; Zhang et al., 2021), which are slightly

younger than what we proposed for the DNCV. If the initiation timing is correct, that further supports that the left-lateral shearing propagated from Vietnam northwestward toward southwestern Tibet, and the extrusion of Indochina coincided with the ridge jumping event rather than the opening event of the SCS.

6 Conclusion

The $^{40}Ar/^{39}Ar$ ages obtained from amphibole (~26 Ma), phlogopite (~25 Ma), muscovites (~24-23 Ma), biotite (~25-23 Ma), and K-feldspars (~25-22 Ma) collected from different structural domains of the DNCV metamorphic massif showed a rapid exhumation between ~26–22 Ma. By incorporating microstructural, petrological, and thermochronological evolution, a temporal-thermal-deformation history was reconstructed. The oldest deformation event D_1 formed NNW-SSE striking vertical axial-plane folds. The mineral assemblage of quartz, K-feldspar, biotite, garnet, and sillimanite indicated metamorphic conditions from granulite facies to upper amphibolite facies possibly occurred before 32 Ma. The second deformation event D_2 relates to sub-horizontal to inclined folds. Mineral assemblages of sillimanite + biotite + high deformed quartz and feldspar suggested that the D_2 deformation event happened between upper to lower amphibolite facies (~650°C–500°C) conditions, possibly during ~32–26 Ma. The last ductile deformation event D_3 was a large-scale doming event associated with left-lateral transpressional shearing. The new precipitation of muscovite and albite within the mylonite belts indicated a greenschist facies metamorphic condition had occurred during shearing. The cooling age of syn-shearing muscovite (~24 Ma) marked the upper bound of the initiation of the left-lateral shear activity. The youngest K-feldspar age (~22 Ma) indicated the termination of the ductile shearing activity as the deformation condition had passed the brittle-ductile transition. This age (~24–22 Ma) coincided with the age of the ridge jump event rather than the initial rifting event in the SCS. Thus, the extrusion tectonism had not caused the initial opening of the SCS. Rather, the SE extrusion of Indochina coincided with the southward ridge jump of the SCS.

Data availability statement

The original contributions presented in the study are included in the article/Supplementary Material, further inquiries can be directed to the corresponding author.

Ethics Statement

Written informed consent was obtained from the individual(s) for the publication of any potentially identifiable images or data included in this article.

Author contributions

The samples were collected by M-WY, T-YL, MK, and RW. Argon analysis are conducted by MK, and RM. Data are

processed by T-HD and M-WY. The MS is mainly composed by T-HD, M-WY, and T-YL. All authors contributed to the article and approved the submitted version.

Funding

Acknowledgments

Conflict of interest

The authors declare that the research was conducted in the absence of any commercial or financial relationships that could be construed as a potential conflict of interest.

Publisher's note

All claims expressed in this article are solely those of the authors and do not necessarily represent those of their affiliated organizations, or those of the publisher, the editors and the reviewers. Any product that may be evaluated in this article, or claim that may be made by its manufacturer, is not guaranteed or endorsed by the publisher.

Supplementary material

The Supplementary Material for this article can be found online at: https://www.frontiersin.org/articles/10.3389/feart.2023.1125279/full#supplementary-material

References

Anczkiewicz, R., Viola, G., Müntener, O., Thirlwall, M. F., Villa, I. M., and Quong, N. Q. (2007). Structure and shearing conditions in the day Nui Con Voi massif: Implications for the evolution of the Red River Shear zone in northern Vietnam. *Tectonics* 26. doi:10.1029/2006TC001972

Ben-Avraham, Z., and Uyeda, S. (1983). Entrapment origin of marginal seas. *Geodyn. West. Pacific-Indonesian Reg.* 11, 91–104.

Briais, A., Patriat, P., and Tapponnier, P. (1993). Updated interpretation of magnetic anomalies and seafloor spreading stages in the south China Sea: Implications for the Tertiary tectonics of Southeast Asia. *J. Geophys. Res. Solid Earth* 98, 6299–6328. doi:10.1029/92JB02280

Burov, E. (2010). *New Frontiers in integrated solid Earth sciences*. Berlin, Germany: Springer. doi:10.1007/978-90-481-2737-5

Carter, A., Roques, D., Bristow, C., and Kinny, P. (2001). Understanding mesozoic accretion in southeast Asia: Significance of triassic thermotectonism (indosinian orogeny) in Vietnam. *Geology* 29, 211214. doi:10.1130/0091-7613(2001)029<0211:UMAISA>2.0.CO;2

Cassel, E. J., Calvert, A. T., and Graham, S. A. (2009). Age, geochemical composition, and distribution of Oligocene ignimbrites in the northern Sierra Nevada, California: Implications for landscape morphology, elevation, and drainage divide geography of the Nevadaplano. *Int. Geol. Rev.* 51 (7-8), 723–742.

Cesare, B., Marchesi, C., and Connolly, J. A. D. (2002). Growth of myrmekite coronas by contact metamorphism of granitic mylonites in the aureole of Cima di Vila, Eastern Alps, Italy. *J. Metamorph. Geol.* 20, 203–213. doi:10.1046/j.0263-4929.2001.00351.x

Christopherson, R. W., Byrne, M.-L., and Aitken, A. E. (2009). *Geosystems: An introduction to physical geography*. Saddle River, New Jersey: Pearson/Prentice Hall Upper.

Chung, S.-L., Lee, T.-Y., Lo, C.-H., Wang, P.-L., Chen, C.-Y., Yem, N. T., et al. (1997). Intraplate extension prior to continental extrusion along the Ailao Shan-Red River shear zone. *Geology* 25, 311. doi:10.1130/0091-7613(1997)025<0311:IEPTCE>2.3

Costa, S., Maluski, H., and Lardeaux, J.-M. (1993). 40Ar-39Ar chronology of variscan tectono-metamorphic events in an exhumed crustal nappe: The monts du Lyonnais complex (massif central, France). *Chem. Geol.* 105, 339–359.

Criss, R. E. (2020). "Chapter 6 - thermal models of the continental lithosphere," in *Heat transport and energetics of the Earth and rocky planets* (Amsterdam, Netherlands: Elsevier), 151–174.

Deino, A. L. (2014). Users manual for Mass Spec v. 7.961. Berkeley Geochronology Center Special Publication 3, 130.

Dinh, T. H., Chan, Y. C., and Chen, C. T. (2022). Extensional tectonics and basement uplift of the fansipan and tule mountain ranges in northern Vietnam. *Front. Earth Sci.* 9, 1–18. doi:10.3389/feart.2021.741670

Dinh, T.-H., Yeh, M.-W., Lee, T.-Y., Kunk, M. J., Wintsch, R. P., McAleer, R. J., et al. (2023). 40Ar/39Ar isotopic data from the Day Nui Con Voi metamorphic massif. *U. S. Geological Survey Data Release*. doi:10.5066/P95TMTH2

Dodson, M. H. (1973). Closure temperature in cooling geochronological and petrological systems. *Contributions Mineralogy Petrology* 40 (3), 259–274.

Dung, P. T., Hoa, T. T., Anh, T. T., Van Hieu, T., Ly, V. H., Ching-Ying, L., et al. (2012). New data of Ye Yen Sun granite complex in Phan Si Pan uplift. *Sci. Earth* 34 (3), 193–204.

Duong, V. H., Trinh, P. T., Nguyen, T. D., Piestrzyski, A., Nguyen, D. C., Pieczonka, J., et al. (2021). Cu-Au mineralization of the sin quyen deposit in north Vietnam: A product of cenozoic left-lateral movement along the Red River Shear zone. *Ore Geol. Rev.* 132, 104065. doi:10.1016/j.oregeorev.2021.104065

Fossen, H. (2016). *Structural geology*. Cambridge, United Kingdom: Cambridge University Press.

Froese, E. (1973). The assemblage quartz–K feldspar–biotite–garnet–sillimanite as an indicator of–T conditions. *Can. J. Earth Sci.* 10, 1575–1579.

Gilley, L. D., Harrison, T. M., Leloup, P. H., Ryerson, F. J., Lovera, O. M., and Wang, J.-H. (2003). Direct dating of left-lateral deformation along the Red River shear zone, China and Vietnam. *J. Geophys. Res. Solid Earth* 108. doi:10.1029/2001JB001726

Girdler, R. W. (1965). The formation of new oceanic crust. *Philos. Trans. R. Soc. Lond. Ser. A, Math. Phys. Sci.* 258, 123–136.

Gou, Q., Qian, X., Wang, Y., Wang, Y., Zhang, Y., and Wang, Y. (2021). Eocene-oligocene crustal thickening-collapse of the eastern Tibetan plateau: Evidence from the potassic granitoids in SW China. *Lithosphere* 2021, 1–34. doi:10.2113/2021/3343655

Hall, R. (2002). Cenozoic geological and plate tectonic evolution of SE Asia and the SW pacific: Computer-based reconstructions, model and animations. *J. Asian Earth Sci.* 20, 353–431. doi:10.1016/S1367-9120(01)00069-4

Hall, R. (1997). Cenozoic plate tectonic reconstructions of SE Asia. *Geol. Soc. Lond. Spec. Publ.* 126, 11–23.

Hall, R. (2009). Southeast Asia's changing palaeogeography. *Blumea-Biodiversity, Evol. Biogeogr. Plants* 54, 148–161.

Harrison, T. M., Leloup, P. H., Ryerson, F. J., Tapponnier, P., Lacassin, R., and Chen, W. (1996). Diachronous initiation of transtension along the ailao Shan-Red River Shear zone, yunnan and Vietnam. *World Reg. Geol.*, 208–226.

Harrison, T. M., and Lovera, O. M. (2014). The multi-diffusion domain model: Past, present and future. *Geol. Soc. Lond. Spec. Publ.* 378 (1), 91–106.

Harrison, T. M., and McDougall, I. (1982). The thermal significance of potassium feldspar K-Ar ages inferred from 40Ar39Ar age spectrum results. *Geochim. Cosmochim. Acta* 46, 1811–1820.

Haugerud, R. A., and Kunk, M. J. (1988). ArAr*; a computer program for reduction of 40Ar-39Ar data. *U.S. Geological Survey Open-file Report* 88–261, 67. doi:10.3133/OFR88261

Jolivet, L., Beyssac, O., Goffé, B., Avigad, D., Lepvrier, C., Maluski, H., et al. (2001). Oligo-Miocene midcrustal subhorizontal shear zone in Indochina. *Tectonics* 20, 46–57. doi:10.1029/2000TC900021

Junlai, L., Xiaoyu, C., Tang, Y. B., Song, Z., and Wang, W. (2020). The Ailao Shan–Red River shear zone revisited:Timing and tectonic implications. *Bull. Geol. Soc. Am.* 132, 1165–1182. doi:10.1130/b35220.1

Karig, D. E. (1971). Origin and development of marginal basins in the Western Pacific. *J. Geophys. Res.* 76, 2542–2561. doi:10.1029/JB076i011p02542

Kelley, S. (2002). Excess argon in K–Ar and Ar–Ar geochronology. *Chem. Geol.* 188 (1-2), 1–22.

Khoi, N. N., Hauzenberger, C. A., Tuan, D. A., Hager, T., Van Nam, N., and Duong, N. T. (2016). Mineralogy and petrology of gneiss hosted corundum deposits from the Day Nui Con Voi metamorphic range, Ailaoshan-Red River shear zone (North Vietnam). *J. Mineralogy Geochem.* 193 (2), 161.

Kuiper, K. F., Deino, A., Hilgen, F. J., Krijgsman, W., Renne, P. R., Wijbrans, J. R., et al. (2008). Synchronizing rock clocks of Earth history. *science* 320 (5875), 500–504.

Kunk, M. J., Wintsch, R. P., Naeser, C. W., Naeser, N. D., Southworth, C. S., Drake, A. A., et al. (2005). Contrasting tectonothermal domains and faulting in the Potomac terrane, Virginia-Maryland - discrimination by 40Ar/39Ar and fission-track thermochronology. *Bull. Geol. Soc. Am.* 117, 1347–1366. doi:10.1130/B25599.1

Lee, J.-Y., Marti, K., Severinghaus, J. P., Kawamura, K., Yoo, H.-S., Lee, J. B., et al. (2006). A redetermination of the isotopic abundances of atmospheric. *Ar. Geochim. Cosmochim. Acta* 70, 4507–4512.

Lee, T.-Y., and Lawver, L. A. (1995). Cenozoic plate reconstruction of southeast Asia. *Tectonophysics* 251, 85–138. doi:10.1016/0040-1951(95)00023-2

Leloup, P. H., Arnaud, N., Lacassin, R., Kienast, J. R., Harrison, T. M., Trong, T. T. P., et al. (2001). New constraints on the structure, thermochronology, and timing of the Ailao Shan-Red River shear zone, SE Asia. *J. Geophys. Res. Solid Earth* 106, 6683–6732. doi:10.1029/2000JB900322

Leloup, P. H., and Kienast, J.-R. (1993). High-temperature metamorphism in a major strike-slip shear zone: The ailao Shan—red River, people's republic of China. *Earth Planet. Sci. Lett.* 118, 213–234. doi:10.1016/0012-821X(93)90169-A

Leloup, P. H., Lacassin, R., Tapponnier, P., Schärer, U., Zhong, D., Liu, X., et al. (1995). The ailao Shan-Red River Shear zone (yunnan, China), tertiary transform boundary of Indochina. *Tectonophysics* 251, 3–84. doi:10.1016/0040-1951(95)00070-4

Leloup, P. H., Tapponnier, P., Lacassin, R., and Searle, M. P. (2007). Discussion on the role of the Red River Shear zone, yunnan and Vietnam, in the continental extrusion of SE Asia. *J. Geol. Soc. Lond.* 164, 12531260. doi:10.1144/0016-76492007-065

Li, C-F., Xu, X., Lin, J., Sun, Z., Zhu, J., Yao, Y., et al. (2014). Ages and magnetic structures of the South China Sea constrained by deep tow magnetic surveys and IODP Expedition 349. *Geochem. Geophys. Geosystems* 15, 4958–4983. doi:10.1002/2014GC005567

Li, J., Cao, S., Neubauer, F., Cheng, X., Wang, H., and Genser, J. (2021). Structure and spatial-temporal relationships of Eocene-Oligocene potassic magmatism linked to the Ailao Shan-Red River shear zone and post-collisional extension. *Lithos* 396–397, 106203. doi:10.1016/j.lithos.2021.106203

Liu, J., Chen, X., Tang, Y., Song, Z., and Wang, W. (2020). The Ailao ShanRed River shear zone revisited: Timing and tectonic implications. *Geol. Soc. Am. Bull.* 132 (5-6), 1165–1182.

Longley, I. M. (1997). The tectonostratigraphic evolution of SE Asia. *Geol. Soc. Lond. Spec. Publ.* 126, 311–339.

Lovera, O. M., Grove, M., and Harrison, T. M. (2002). Systematic analysis of K-feldspar 40Ar/39Ar step heating results II: Relevance of laboratory argon diffusion properties to nature. *Geochimica Cosmochimica Acta* 66 (7), 1237–1255.

Lovera, O. M., Richter, F. M., and Harrison, T. M. (1991). Diffusion domains determined by 39 Ar released during step heating. *J. Geophys. Res.* 96, 2057. doi:10.1029/90JB02217

Mai, H. A., Chan, Y. L., Yeh, M. W., and Lee, T. Y. (2018). Tectonic implications of Mesozoic magmatism to initiation of Cenozoic basin development within the passive South China Sea margin. *Int. J. Earth Sci.* 107, 1153–1174. doi:10.1007/s00531-017-1537-y

Min, K., Mundil, R., Renne, P. R., and Ludwig, K. R. (2000). A test for systematic errors in 40Ar/39Ar geochronology through comparison with U/Pb analysis of a 1.1–Ga rhyolite. *Geochim. Cosmochim. Acta* 64, 73–98.

Morley, C. K. (2002). A tectonic model for the Tertiary evolution of strike–slip faults and rift basins in SE Asia. *Tectonophysics* 347, 189–215.

Nam, T. N., Toriumi, M., and Itaya, T. (1998). P-T-t paths and post-metamorphic exhumation of the Day Nui Con Voi shear zone in Vietnam. *Tectonophysics* 290, 299–318. doi:10.1016/S0040-1951(98)00054-7

Palin, R. M., Searle, M. P., Waters, D. J., Parrish, R. R., Roberts, N. M. W., Horstwood, M. S. A., et al. (2013). A geochronological and petrological study of anatectic paragneiss and associated granite dykes from the Day Nui Con Voi metamorphic core complex, North Vietnam: Constraints on the timing of metamorphism within the Red River shear zone. *J. Metamorph. Geol.* 31, 359–387. doi:10.1111/jmg.12025

Regard, V., Carretier, S., Boeglin, J., Ndam Ngoupayou, J., Dzana, J., Bedimo Bedimo, J., et al. (2016). Denudation rates on cratonic landscapes: Comparison between suspended and dissolved fluxes, and 10Be analysis in the Nyong and Sanaga River basins, South Cameroon. *Earth Surf. Process. Landforms* 41, 1671–1683.

Schaen, A. J., Jicha, B. R., Hodges, K. V., Vermeesch, P., Stelten, M. E., Mercer, C. M., et al. (2020). Interpreting and reporting 40 Ar / 39 Ar geochronologic data. *Geol. Soc. Am. Bull.* 133 (3–4), 461–487. doi:10.1130/B35560.1/5084442/b35560.pdf

Schmitz, M. D. (2012). "Radiogenic isotope geochronology," in *The geologic time scale 2012*. Editors F. M. Gradstein, J. G. Ogg, M. D. Schmitz, and G. M. Ogg (Boston, Massachusetts: Elsevier), 115–126. doi:10.1016/B978-0-444-59425-9.00006-8

Searle, M. P. (2006). Role of the Red River Shear zone, yunnan and Vietnam, in the continental extrusion of SE Asia. *J. Geol. Soc. Lond.* 163, 1025–1036. doi:10.1144/0016-76492005-144

Searle, M. P., Yeh, M.-W., Lin, T.-H., and Chung, S.-L. (2010). Structural constraints on the timing of left-lateral shear along the Red River Shear zone in the ailao Shan and Diancang Shan ranges, yunnan, SW China. *Geosphere* 6, 316–338. doi:10.1130/GES00580.1

Shellnutt, J. G., Pham, T. T., Denyszyn, S. W., Yeh, M. W., and Tran, T. A. (2020). Magmatic duration of the Emeishan large igneous province: Insight from northern Vietnam. *Geology* 48, 457–471. doi:10.1130/G47076.1

Spear, F. S., Kohn, M. J., and Cheney, J. T. (1999). P-T paths from anatectic pelites. *Contrib. Mineral. Pet* 134, 17–32. doi:10.1007/s004100050466

Sun, W. (2016). Initiation and evolution of the South China sea: An overview. *Acta Geochim.* 35, 215–225. doi:10.1007/s11631-016-0110-x

Tapponnier, P., Peltzer, G., and Armijo, R. (1986). On the mechanics of the collision between India and Asia. *Geol. Soc. Lond. Spec. Publ.* 19, 113–157. doi:10.1144/GSL.SP.1986.019.01.07

Tapponnier, P., Peltzer, G., Le Dain, A. Y., Armijo, R., and Cobbold, P. (1982). Propagating extrusion tectonics in Asia: New insights from simple experiments with plasticine. *Geology* 10, 611–616. doi:10.1130/0091-7613(1982)10<611:PETIAN>2.0

Taylor, B., and Hayes, D. E. (1980). *The tectonic evolution of the South China Basin*. Washington, D.C., United States: American Geophysical Union AGU, 89–104. doi:10.1029/GM023p0089

Usuki, T., Lan, C.-Y., Tran, T. H., Pham, T. D., Wang, K.-L., Shellnutt, G. J., et al. (2015). Zircon U–Pb ages and Hf isotopic compositions of alkaline silicic magmatic rocks in the Phan Si Pan-Tu Le region, northern Vietnam: Identification of a displaced Western extension of the Emeishan Large Igneous Province. *J. Asian Earth Sci.* 97, 102–124. doi:10.1016/J.JSEAES.2014.10.016

Villa, I. M. (2014). Diffusion of Ar in K-feldspar: Present and absent. *Geol. Soc. Lond. Spec. Publ.* 378 (1), 107–116.

Viola, G., and Anczkiewicz, R. (2008). Exhumation history of the Red River shear zone in northern Vietnam: New insights from zircon and apatite fission-track analysis. *J. Asian Earth Sci.* 33, 78–90. doi:10.1016/j.jseaes.2007.08.006

Wang, E., and Burchfiel, B. C. (1997). Interpretation of Cenozoic tectonics in the right-lateral accommodation zone between the Ailao Shan shear zone and the eastern Himalayan syntaxis. *Int. Geol. Rev.* 39, 191219. doi:10.1080/00206819709465267

Wang, P. L., Lo, C. H., Lee, T. Y., Chung, S. L., Lan, C. Y., and Yem, N. T. (1998). Thermochronological evidence for the movement of the ailao Shan-Red River Shear zone: A perspective from Vietnam. *Geology* 26, 887–890. doi:10.1130/0091-7613(1998)026<0887:TEFTMO>2.3

Wang, P.-L., Lo, P.-H., Chung, S. L., Lee, T.-Y., Lan, C.-Y., Thang, T. V., et al. (2000). Onset timing of left-lateral movement along the Ailao ShanRed River Shear Zone: 40Ar/39Ar dating constraint from the Nam Dinh Area, northeastern Vietnam. *J. Asian Earth Sci.* 18 (3), 281–292. Elsevier. Available at:https://www.sciencedirect.com/science/article/pii/S1367912099000644 (Accessed October 23, 2018).

Wirth, R., and Voll, G. (1987). Cellular intergrowth between quartz and sodium-rich plagioclase (myrmekite) - an analogue of discontinuous precipitation in metal alloys. *J. Mat. Sci.* 22, 1913–1918. doi:10.1007/BF01132916

Wu, W., Liu, J., Zhang, L., Qi, Y., and Ling, C. (2017). Characterizing a middle to upper crustal shear zone: Microstructures, quartz c-axis fabrics, deformation temperatures and flow vorticity analysis of the northern Ailao Shan-Red River shear zone, China. *J. Asian Earth Sci.* 139, 95–114.

Ye, Q., Mei, L., Shi, H., Camanni, G., Shu, Y., Wu, J., et al. (2018). The Late Cretaceous tectonic evolution of the South China Sea area: An overview, and new perspectives from 3D seismic reflection data. *Earth-Science Rev.* 187, 186–204. doi:10.1016/j.earscirev.2018.09.013

Yeh, M.-W., Lee, T.-Y., Lo, C.-H., Chung, S.-L., Lan, C.-Y., and Anh, T. T. (2008). Structural evolution of the day Nui Con Voi metamorphic complex: Implications on the development of the Red River Shear zone, northern Vietnam. *J. Struct. Geol.* 30, 1540–1553. doi:10.1016/J.JSG.2008.08.007

Yeh, M. W., Wintsch, R. P., Liu, Y. C., Lo, C. H., Chung, S. L., Lin, Y. L., et al. (2014). Evidence for cool extrusion of the north Indochina block along the ailao Shan Red River Shear zone, a Diancang Shan perspective. *J. Geol.* 122, 567–590. doi:10.1086/677263

Zhang, B., Chen, S. Y., Wang, Y., Reiners, P. W., Cai, F. L., Speranza, F., et al. (2021). Crustal deformation and exhumation within the India-Eurasia oblique convergence zone: New insights from the Ailao Shan-Red River shear zone. *GSA Bull* doi:10.1130/b35975.1

Zhang, L.-S., and Schärer, U. (1999). Age and origin of magmatism along the Cenozoic Red River shear belt, China. *Contrib. Mineral. Pet.* 134, 67–85. doi:10.1007/s004100050469